Leaching of magnesium potassium phosphate cement pastes under alkaline conditions

Laura Diaz Caselles, Céline Cau Dit Coumes, Pascal Antonucci, Angélique Rousselet, Adel Mesbah, Valérie Montouillout

Leaching of magnesium potassium phosphate cement pastes under alkaline conditions

Laura Diaz Caselles [1*], Céline Cau Dit Coumes [1], Pascal Antonucci [1], Angélique Rousselet [2], Adel Mesbah [3], Valérie Montouillout [4]

[1] *CEA, DES, ISEC, DPME, SEME, LFCM, Univ Montpellier, Marcoule, France*
[2] *Université Paris-Saclay, CEA, Service de recherche en Corrosion et Comportement des Matériaux, 91191, Gif-sur-Yvette, France*
[3] *Univ Lyon, Université Lyon 1, Institut de Recherches sur la Catalyse et l'Environnement de Lyon, IRCELYON, UMR5256, CNRS, Villeurbanne, France*
[4] *CNRS, CEMHTI UPR3079, Univ. Orléans, F-45071 Orléans, France*
[*] Corresponding Author, E-mail: lauradiazcaselles@gmail.com

Abstract

Some legacy radioactive waste containing aluminum (Al) metal need to be stabilized and solidified before their final disposal. Currently, Portland cement (PC) is extensively used for conditioning low- or intermediate-level radioactive waste. However, the high alkalinity of PC leads to strong corrosion of Al metal, which is associated with significant dihydrogen release. Therefore, it is important to investigate alternative binders that show better chemical compatibility with Al metal. Magnesium potassium phosphate cements (MKPCs), comprising equimolar amounts of MgO and KH_2PO_4, are interesting candidates since their pore solution pH may fall within the passivation domain of Al metal. The understanding of their long-term durability, especially under alkaline conditions, is however incomplete. Hence, MKPC paste samples (with fly ash as a filler) were submitted to semi-dynamic leaching tests using an alkaline solution under well-controlled conditions. The leachates were analyzed over time using ICP-AES, and the leached solids were characterized by XRD, SEM/EDS, and ^{31}P MAS-NMR spectroscopy. Leaching induced a decrease in the content of crystalline K-struvite ($MgKPO_4 \cdot 6H_2O$), the main hydrate of the paste samples, as well as the precipitation of Ca-deficient hydroxyapatite (CDHA), brucite ($Mg(OH)_2$) and possibly magnesium silicate hydrates. The experimental data were then used as an input for numerical simulations using the reactive transport code HYTEC.

Keywords: magnesium phosphate cement; durability; alkaline leaching; modeling; hydroxyapatite

1. Introduction

Magnesium phosphate cements (MPCs) are alternative binders to Portland cement (PC) and form through the reaction between magnesium oxide (MgO) and an acidic phosphate salt, such as potassium dihydrogen phosphate (KH_2PO_4), sodium dihydrogen phosphate (NaH_2PO_4) or ammonium dihydrogen phosphate ($NH_4H_2PO_4$) (Wagh, 2013; Wagh et al., 1997; Weill and Bradik, 1988; Xu et al., 2018). The binder is referred to as magnesium potassium phosphate cement (MKPC) when KH_2PO_4 is used as the phosphate source. In contact with water, dissolution and precipitation processes take place, mainly yielding K-struvite ($MgKPO_4 \cdot 6H_2O$). Secondary products such as bobierrite ($Mg_3(PO_4)_2 \cdot 8H_2O$), cattiite ($Mg_3(PO_4)_2 \cdot 22H_2O$) or brucite ($Mg(OH)_2$) may also form depending on the raw materials and the formulation used (e.g., water-to-cement ratio, Mg/P molar ratio, addition of retarders) (Ding et al., 2012; Lahalle et al., 2018; Lothenbach et al., 2019; Xu et al., 2019, 2018). When the cement initially contains equimolar amounts of MgO and KH_2PO_4, phases such as newberyite ($MgHPO_4.3H_2O$), phosphörrosslerite ($MgHPO_4.7H_2O$) and $Mg_2KH(PO_4)_2.15H_2O$ may precede the formation of K-struvite (Chau et al., 2012; Ding et al., 2012; Lahalle, 2016; Lahalle et al., 2018; Le Rouzic et al., 2017) and the pore solution pH rapidly increases from 4.2 to a value close to 8.

MPCs are of interest in civil engineering applications, such as road repairing, due to their fast setting and good bonding properties (Arora et al., 2019; Li et al., 2014; Seehra et al., 1993), but also for bioengineering (Yu et al., 2016, 2010; Zhang et al., 2018) and 3D printing (Weng et al., 2019; Zhao et al., 2021). They are also investigated as conditioning agents for toxic and/or radioactive waste (Buj et al., 2010; Pyo et al., 2021; Torras et al., 2011). Thanks to their low alkalinity, these binders may indeed offer new prospects for the stabilization/solidification of waste that is unstable in basic environment. This is the case for aluminum (Al) metal, which can be encountered in legacy radioactive waste (Cau Dit Coumes et al., 2014; Ionascu et al., 2014; Poras et al., 2023). At high pH, Al metal is strongly corroded, with simultaneous production of dihydrogen, an explosive gas whose accumulation may raise safety issues in a disposal. Several authors (Cau Dit Coumes et al., 2014; Langton and Stefanko, 2011; Perona et al., 2023; Poras et al., 2023) have shown that the H_2 outgassing

of cemented waste packages containing Al metal can be strongly reduced by using MKPC (with a Mg/P molar ratio set at 1) instead of PC.

Information on the long-term evolution of MKPC-based materials is still limited, especially under the alkaline conditions that may be encountered in the near field of a conventional concrete produced with PC or composite cement (Braney et al., 1993). A few studies have shown that immersion of MKPC samples in alkaline solution may induce some microstructural and mineralogical changes (Lahalle et al., 2019; Yang et al., 2000). For instance, Lahalle et al., 2019 investigated the evolution over time of MKPC pastes (Mg/P molar ratio of 1) immersed in an alkaline solution mimicking the pore solution of a concrete prepared with PC blended with fly ash and blast furnace slag. The solution had a pH close to 13.2 and contained K (133 mmol/L), Na (from 66 to 107 mmol/L) and Ca (1 mmol/L) ions, as well as chlorides (40 mmol/L) in some cases. A decrease in the content of crystalline K-struvite was observed as well as the precipitation of brucite. The increase in the amorphous content was also observed, likely due to the amorphization of existent K-struvite, but also to the formation of another mineral, responsible for a hump in 10°-12° 2θ range, and still unassigned. The authors also suggested the possible substitution of K^+ by Na^+ in the structure of K-struvite, leading to the formation of hazenite ($Mg_2KNa(PO_4)_2 \cdot 14H_2O$). Furthermore, the pore solution pH of the cement pastes increased from 8 to 11-12. In a recent study, Xu et al., 2023 used thermodynamic modeling to predict the evolution of MKPC pastes (Mg/P molar ratio of 4) exposed to alkaline solutions. K-struvite was calculated to dissolve partly to form brucite and hazenite, which was then confirmed experimentally.

Some questions remain however concerning the rate of degradation of MKPC-based materials and the mechanisms controlling this degradation under such alkaline conditions. This work thus investigates the durability of MKPC pastes using semi-dynamic leaching tests previously developed to understand and model the degradation processes of PC hydrates (Adenot and Buil, 1992). For this purpose, MKPC pastes were prepared using equimolar amounts of MgO and KH_2PO_4 and fly ash as a filler. Samples were cured for 6 months under endogenous conditions. Leaching experiments were then launched on monolithic samples under well-controlled conditions (pH, temperature, composition of the aggressive solution), with careful analysis of both the leachates and the leached solids. Based on

these results, a first modeling approach was then proposed, aiming at predicting the mineralogical evolutions in MKPC pastes exposed to leaching by an alkaline solution.

2. Materials and Methods

2.1. Materials

Table 1 presents the chemical composition of the raw materials, determined by semi-quantitative X-ray fluorescence (XRF). A hard-burnt magnesium oxide (MgO) was obtained from Martin Marietta Magnesia specialties (MagChem® 10CR, purity above 98.3%). The MgO displayed a monomodal particle size distribution (d_{10} = 4.8 µm, d_{50} = 18.9 µm, and d_{90} = 45.6 µm), along with a specific surface area (BET) of 0.9 m^2/g. Potassium dihydrogen phosphate (KH_2PO_4) (d_{10} = 139 µm, d_{50} = 303 µm, and d_{90} = 566 µm) was supplied by YARA (KH_2PO_4 KristaTM) and had a purity above 98%. A low calcium oxide fly ash (siliceous fly ash V, according to EN 197-1) (d_{10} = 7 µm, d_{50} = 31 µm, and d_{90} = 163 µm, specific surface area (BET) of 1.5 m^2/g) was obtained from EDF (power station at Cordemais, France) and comprised 10.4 wt. % quartz, 17.2 wt. % mullite, and 72.4 wt. % amorphous content, as determined XRD Rietveld analysis. Boric acid $B(OH)_3$ (purity above 98%) was purchased from VWR.

Table 1 – Chemical composition of the raw materials, obtained by semi-quantitative XRF (% by weight).

	SiO_2	Al_2O_3	Fe_2O_3	CaO	K_2O	TiO_2	Na_2O	MgO	P_2O_5	SO_3	Cl^-
MgO	0.3	-	0.3	0.9	-	-	-	98.5	-	-	-
KH_2PO_4	-	-	-	-	40.0	-	-	-	59.3	0.5	0.1
Fly ash	57.8	24.7	6.0	4.5	2.2	1.3	0.7	1.6	0.6	0.5	0.1

2.2. Preparation and curing of paste samples

The samples were prepared as described in Diaz Caselles et al., 2024, meaning that a MgO/KH_2PO_4 molar ratio equal to 1 and a water-to-cement (w/c) weight ratio of 0.51 were used. “Cement” denotes the combination of MgO and KH_2PO_4. Such w/c ratio corresponds to the stoichiometry of the overall reaction yielding K-struvite (Eq. 1):

$$MgO + KH_2PO_4 + 5\ H_2O \rightarrow MgKPO_4.6H_2O \qquad Eq.\ 1$$

To improve the rheological properties and paste stability in the fresh state, fly ash (FA) was added to the mixture, while $B(OH)_3$ was incorporated as a set retarder. The weight ratios of FA/c and $B(OH)_3$/c were set to 1 and 0.02, respectively. For the preparation of the samples, $B(OH)_3$ was first diluted in demineralized water using a closed reactor and a magnetic stirrer. Then, pre-mixed dried solids (MgO, KH_2PO_4 and FA) were mixed with the $B(OH)_3$ solution for 5 minutes in a 3-L mixer, according to EN 196-1. The paste was cast into cylindrical plastic molds of 8 cm in length and 5 cm in diameter, which were tightly closed to avoid desiccation. The molds were then placed in a controlled chamber at 20 °C for the endogenous curing. Table 2 presents the mix composition of the paste samples.

Table 2 - Mix composition of MKPC paste samples. Values are given in grams per 1 L of material.

	MgO	**KH_2PO_4**	**Fly ash**	**Boric acid**	**Water[a]**	**w/c[b]**
MKPC paste	131.4	443.6	575.0	11.5	293.2	0.51

[a] Demineralized water; [b] Water-to-cement weight ratio (cement: $MgO+KH_2PO_4$).

2.3. Methods

2.3.1. Semi-dynamic leaching tests

Two semi-dynamic leaching tests were performed on paste monoliths for periods of 14 days and 170 days using an alkaline solution. The resulting leached solids will be referred to as MKP-14d and MKP-170d, respectively.

The leaching solution was prepared to mimic the pore solution of a conventional concrete prepared with PC blended with blast furnace slag and fly ash. The composition was simplified by neglecting trace elements. First, demineralized water was boiled for 1 hour at 105 °C to eliminate carbon dioxide (CO_2), followed by cooling under nitrogen atmosphere. The decarbonated water was then mixed with 0.05 mol/L NaOH, 0.15 mol/L KOH (86%), and 0.001 mol/L CaO (obtained by calcining calcium hydroxide ($Ca(OH)_2$) in a furnace at 1000 °C for 8 hours to remove any carbonate traces). Once the reactants were dissolved, the solution pH reached a value of 13.2±0.1 at 25 °C.

The monolithic MKPC paste samples (one per test) were suspended in double-walled reactors (Figure 1). To get unidirectional diffusion through the samples, the lateral surface of the monoliths was covered with an epoxy resin, leaving only the parallel end faces exposed (Figure 1). The liquid volume-to-solid surface (L/S) ratio was set at 43.29 cm, and the leaching solution was maintained at 25 °C. To prevent carbonation, nitrogen-saturated water was injected by bubbling into the solution. The leaching solution was regularly renewed to prevent the accumulation of species, and magnetic stirring was applied throughout the tests to maintain uniform concentration levels. For the 14-day test, the leaching solution was renewed at 2, 4, 7 and 10 days. For the 170-day test, renewals were carried out at 2, 6, 14, 22, 42, 51, 59, 69, 77, 85, 94, 101, 107, 115, 127, 135, 143, 156, and 163 days. After each renewal, the pH was measured in the leachates, and the solutions were then diluted by factors of 10, 100, and 500 using diluted HNO_3 (2 vol. % HNO_3 in ultrapure water, 18.2 MΩ.cm). All solutions were stored at 4 °C until ICP-AES analyses were conducted.

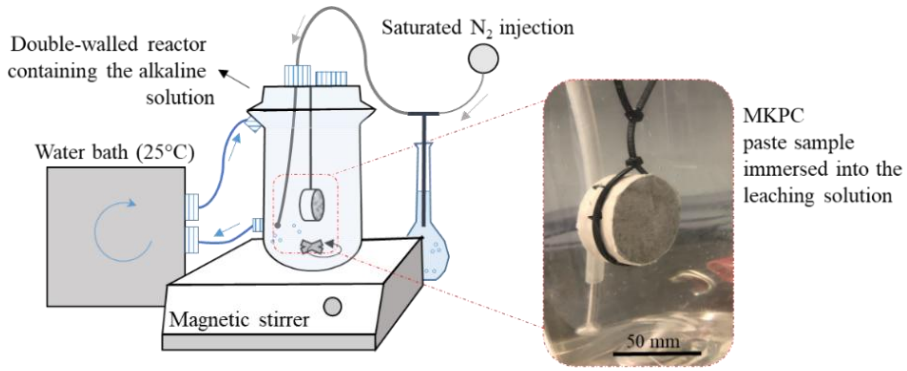

Figure 1 – Scheme of the device used to perform the semi-dynamic leaching tests under alkaline condition.

2.3.2. Hydration stoppage

For the mineralogical and microstructural characterizations, hydration stoppage was performed on pastes after 6 months of curing by solvent exchange using isopropanol and following the RILEM TC-238 SCM guidelines (Snellings et al., 2018). Residual isopropanol was removed by placing the samples in a desiccator at 20 °C and 20 %R.H. for 7 days. After leaching, MKPC pastes were simply rinsed with isopropanol.

2.3.3. X-ray diffraction analyses

XRD analyses were performed as described in Diaz Caselles et al., 2024. Therefore, analyses were carried out on powder samples (particle size inferior to 63 μm). After leaching, powders were obtained at various depths of the sample by scratching, step-by-step, starting from the exposed surface towards the sound core. The thickness difference was determined with a digital caliper having a measurement range of 0-25 mm and an accuracy of 0.001 mm. A PANalytical X'Pert Pro diffractometer with a copper radiation source (Cu Kα, λ = 1.54 Å) and a PIXCel detector was used. Analyses were performed in transmission mode using a capillary (external diameter of 0.7 mm and wall thickness of 0.01 mm). The anode voltage was set at 40 kV with an electric current intensity of 40 mA. Scans were performed over a 5 ° to 120 ° 2θ angular range, with a step size of 2θ 0.013 ° and a time per step of 2.35 s. Pure silicon (Si) was used to extract the instrumental function. Approximately 10 wt.% Si was added to each sample to evaluate the amounts of crystalline phases and amorphous. Diffrac.Suite Eva and/or Highscore softwares were used for identification of phases. The Rietveld refinement was performed using the Fullprof_suite program (Frontera and Rodríguez-Carvajal, 2003). The weight percent content of each phase was evaluated after extracting its structure from the ICSD database and performing Rietveld refinement.

2.3.4. SEM/EDS analyses and optical microscopy

Microstructure analyses were conducted on carbon-coated polished sections, previously soaked into isopropanol, and embedded in resin, using a Scanning Electron Microscope (SEM) FEI Inspect S50 equipped with an Electron dispersive spectroscopy (EDS) detector (Bruker XFlash SDD 10 mm^2). Images were obtained in backscattered electron (BSE) configuration at magnifications ranging from 50x to 2,000x. 150 EDS point analyses were performed per sample. For quantification, EDS calibration was conducted using eleven reference standards: $NaAl(Si_2O_6)$, MgO (99.95% pure), Al_2O_3 (99.8% pure), $KAlSi_3O_8$, $CaSiO_3$, Ti (99.99% pure), Cr (99.96% pure), Mn (99.99%), Fe (99.95% pure), FeS_2, and GaP (99.99% pure). Moreover, pastes were characterized by optical microscopy using

a 4K high accuracy digital microscope (Keyence VHX-7000) combining large depth of filed and high resolution.

2.3.5. ^{31}P MAS-NMR spectroscopy

Changes in the P environment in the MKPC pastes were investigated by solid state magic angle spinning nuclear magnetic resonance (MAS NMR). ^{31}P spectra were acquired on a Bruker AVANCE III spectrometer (B_0 = 9.4 T) operating at 162 MHz. The spinning speed was fixed at 20 kHz and 384 scans were accumulated after a single short pulse ($\pi/4$) and a recycling delay of 360 s to ensure complete magnetization relaxation. 2.5 mm zirconia rotors were employed. The chemical shifts were referenced relative to H_3PO_4 85%, and quantitative analyses were performed using the Dmfit program developed at CEMHTI (Massiot et al., 2002).

2.3.6. Raman spectroscopy

Raman spectroscopy was used to investigate vibrational modes. Analyses were performed on powder samples using a Raman XploRA Plus (Horiba) equipped with a Syncerity detector (cooled down at -60°C). Raman spectra were recorded in the 1800-50 cm^{-1} range using 10 accumulations per scan with an acquisition time of 20 s per accumulation. The pairing of laser wavelength and diffraction grating used was 532 nm-1800 gr/mm, with a laser intensity set at 100%.

2.3.7. Porosity characterization

Porosity accessible to water was determined as described in Diaz Caselles et al., 2024 and following European Standard NF P 18-459 (2022). Three cylindrical paste samples (2 cm high and 5 cm in diameter) were used after 6 months of curing and before leaching. First, the samples were placed in a vacuum desiccator at 25 mbar for 4 hours. Then, they were covered with demineralized water while maintaining the 25 mbar vacuum pressure for a minimum of 44 hours. Drying was conducted in a controlled chamber at 38 °C and 10% R.H. to prevent K-struvite dehydration (Lahalle et al., 2019; Lothenbach et al., 2019). Arithmetic average result is presented with a 95% confidence interval.

2.3.8. pH estimation

The Rainbow indicator was purchased from German Instruments. This indicator was used to estimate the pH of cement pastes before and after leaching. The color of this indicator changes from orange (pH 4-6) to yellow (pH 6-8), green (pH 8-10), purple (pH 10-12), and blue (pH 12-14). To assess the pH of the paste samples, the indicator was applied to the cross-section of either fractured pieces or sliced samples. Pictures of the sprayed surfaces were taken several minutes later once the indicator solution had dried.

2.3.9. Modeling

One-dimension (1D) model (i.e., unidirectional diffusion) was used to simulate the leaching of MKPC paste. Modeling was performed using reactive transport code HYTEC (version 4.7.4) (van der Lee et al., 2003) as described in Diaz Caselles et al., 2024. General Eq. 2 describes the concentration variation of species *i* in a unit volume, taking into account transport by diffusion through the pore network, and participation to chemical reactions (using the geochemical module CHESS) (De Windt and Badreddine, 2007).

$$\frac{\partial \omega c_i}{\partial t} = \nabla . (D_e \nabla c_i) - \frac{\partial \omega \bar{c_i}}{\partial t} \qquad \textit{Eq. 2}$$

c_i and $\bar{c_i}$ are the mobile and immobile concentrations of a specie per unit volume. ω and D_e are the porosity and the effective diffusion coefficient, respectively. Transport and chemistry are coupled through a sequential iterative algorithm, which simultaneously considers the altered layers due to mineral dissolution, and the associated ion release from the cement paste. Furthermore, changes in local porosity due to dissolution or precipitation of minerals lead to changes in D_e. The retroactive effect of chemistry on mass transport is incorporated through the implementation of a modified version of Archie's law, as described by Eq. 3 (De Windt and Badreddine, 2007).

$$D_e(\omega) = D_e(\omega_0) \left(\frac{\omega - \omega_c}{\omega_0 - \omega_c}\right)^{\alpha} \qquad \textit{Eq. 3}$$

ω_0 is the initial porosity and ω_c is the critical porosity threshold under which diffusion stops (considered as zero in the model). α is an empirical Archie's coefficient, which commonly ranges from

1.5 to 4.0 in the modeling of cementitious materials under leaching (Adenot and Buil, 1992; De Windt and Badreddine, 2007; De Windt and Devillers, 2010; Neithalath et al., 2006). In this study, the Archie's power was set to 2.0.

The computational domain was defined by two zones as presented by Diaz Caselles et al., 2024 (cf. Fig. 2). This means that zone I corresponded to the MKPC paste sample, and zone II to the reactor containing the alkaline leaching solution. The experimental liquid volume-to-solid surface (L/S) ratio of 43.29 cm was reproduced by the geometry definition of each domain (note that the code assumes a depth of 1 m in the z-axis). The node sizes were set at 100 µm in the paste and in the first 10 mm of the reactor (zone B in Fig. 2 in Diaz Caselles et al., 2024). The node size in the rest of the reactor (zone C) was set at 1 mm. The leaching solution comprised 0.13 mol/L KOH, 0.05 mol/L NaOH and 0.001 mol/L portlandite, to obtain the same concentrations as in the experimental leaching solution. The diffusivity coefficient of the leaching solution was set at 1.0×10^{-7} $m^2 \cdot s^{-1}$, and 1.0×10^{-5} $m^2 \cdot s^{-1}$ in the zones B and C to simulate an agitated solution, and to reduce the computation time. No boundary conditions were defined in this model. Additionally, the leaching solution was renewed at the same frequency as in the leaching experiments. The chemical reactions were computed by assuming local thermodynamic equilibrium and utilizing the B-dot model for the calculation of activity coefficients due to the high values of ionic strength (superior to 1).

For this simulation, the thermodynamic CHESS database (version 2.5) was used and enriched with thermodynamic data for magnesium phosphate phases presented by Lothenbach et al., 2019, Xu et al., 2020, and Xu et al., 2023. The minerals considered in the model are presented in Table 3.

Table 3 – Thermodynamic data at 25 °C and 1 bar.

Species	Reaction	Log $K_{formation}$	Vol (kg/m^3)	Ref.
K-struvite	$Mg^{2+} + HPO_4^{2-} + K^+ + 6H_2O \rightarrow MgKPO_4 \cdot 6H_2O + H^+$	-1.36	1870.2	(Lothenbach et al., 2019)
Cattiite	$3Mg^{2+} + 2HPO_4^{2-} + 22H_2O \rightarrow Mg_3(PO_4)_2.22H_2O + 2H^+$	-1.61	1640.5	(Lothenbach et al., 2019)
$Mg_2KH(PO_4)_2.15H_2O$	$2Mg^{2+} + 2HPO_4^{2-} + K^+ + 15H_2O \rightarrow Mg_2KH(PO_4)_2.15H_2O + H^+$	4.03	1810.6	(Lothenbach et al., 2019)
Phosphorrösslerite	$Mg^{2+} + HPO_4^{2-} + 7H_2O \rightarrow MgHPO_4.7H_2O$	4.69	1740.3	(Lothenbach et al., 2019)
Newberyite	$Mg^{2+} + HPO_4^{2-} + 3H_2O \rightarrow MgHPO_4.3H_2O$	5.61	2121.1	(Lothenbach et al., 2019)
$MgKPO_4.H_2O$	$Mg^{2+} + HPO4^{2-} + K^+ + H_2O \rightarrow MgKPO_4.H_2O + H^+$	-1.37	2668.7	(Lothenbach et al., 2019)

Farringtonite	$3Mg^{2+} + 2HPO_4^{2-} \rightarrow Mg_3(PO_4)_2 + 2H^+$	-2.23	2761.2	(Lothenbach et al., 2019)
Bobierrite	$3Mg^{2+} + 2HPO_4^{2-} + 8H_2O \rightarrow Mg_3(PO_4)_2 \cdot 8H_2O + 2H^+$	0.66	2129.9	(Lothenbach et al., 2019)
Magnesium orthophosphate tetrahydrate	$3Mg^{2+} + 2HPO_4^{2-} + 4H_2O \rightarrow Mg_3(PO_4)_2 \cdot 4H_2O + 2H^+$	-1.14	2380.6	(Lothenbach et al., 2019)
$CaK_3H(PO_4)_2$	$Ca^{2+} + 3K^+ + 2HPO_4^{2-} \rightarrow CaK_3H(PO_4)_2 + H^+$	2.24		(Xu et al., 2020)
brucite ($Mg(OH)_2$)	$Mg^{2+} + 2H_2O \rightarrow Mg(OH)_2 + 2H^+$	-16.29	2367.83	Chess v.2.5
Hydroxyapatite	$3HPO_4^{2-} + 5Ca^{2+} + H_2O \rightarrow Ca_5(PO_4)_3(OH) + 4H^+$	7.56		(Janot and Ilschner, 2001)
Hazenite	$2Mg^{2+} + Na^+ + K^+ + 2HPO_4^{2-} + 14H_2O \rightarrow Mg_2NaK(PO_4)_2 \cdot 14H_2O + 2H^+$	-0.64		(Xu et al., 2023)
OCP	$8Ca^{2+} + 6HPO_4^{2-} + 5H_2O \rightarrow Ca_8H_2(PO_4)_6 \cdot 5H_2O + 4H^+$	22.87		(Janot and Ilschner, 2001)
CDHA	$9Ca^{2+} + 6HPO_4^{2-} + H_2O \rightarrow Ca_9(HPO_4)(PO_4)_5OH + 6\ H^+$	12.79		(Janot and Ilschner, 2001)
Portlandite	$Ca^{2+} + 2H_2O \rightarrow Ca(OH)_2 + 2H^+$	-22.80	2245	Chess v2.5

3. Experimental results

3.1. Reference paste characterization

The MKPC paste sample after curing and before leaching was the reference material and is referred to as MKP-ref. Figure 2 presents its XRD pattern after 6 months of endogenous curing.

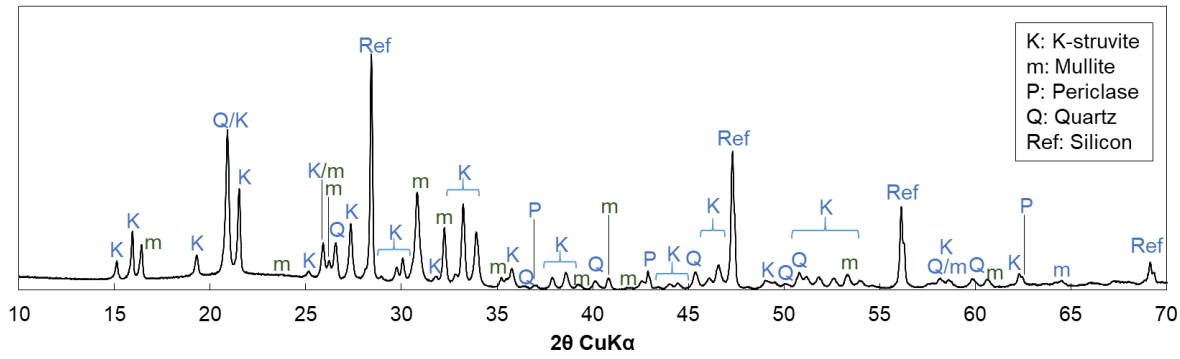

Figure 2 – XRD pattern of MKP-ref plotted in the selected range 10 °-70 ° 2θ.

MKP-ref was composed of K-struvite ($MgKPO_4 \cdot 6H_2O$), along with residual MgO (periclase), quartz, mullite (an alumino-silicate mineral), and an amorphous content (Figure 2). The presence of quartz and mullite were attributed to fly ash. The amorphous content is likely associated with the glassy structure of the fly ash and potentially with the presence of amorphous phosphate phases (e.g.,

amorphous K-struvite, boro-phosphates) (Ding et al., 2012; Lahalle et al., 2019). The mineralogical assemblage of the paste was estimated by Rietveld refinement and comprised 53.8% K-struvite, 33.6 wt.% amorphous, 8.2 wt.% mullite, 2.6 wt.% quartz, and 1.8 wt.% periclase (Diaz Caselles et al., 2024). Therefore, the mullite-to-quartz ratio was 3.

Figure 3 shows the ^{31}P MAS-NMR spectrum obtained from MKP-ref after 6 months of curing (see spectrum in the top), and Table 4 presents the quantitative estimations resulting from the decomposition of ^{31}P MAS-NMR spectra (Diaz Caselles et al., 2024).

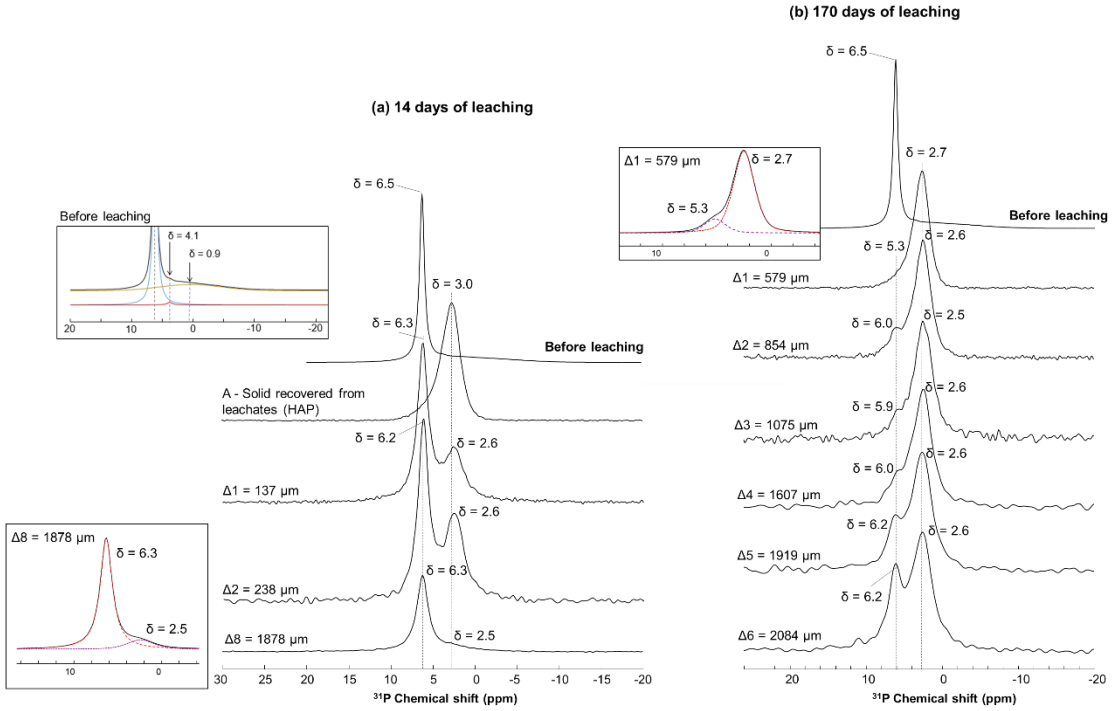

Figure 3 – ^{31}P MAS-NMR spectra obtained before (MKP-ref), and after leaching (MKP-14d and MKP-170d). δ indicates the chemical shift.

Table 4 - ^{31}P site fractions (mol. %) estimated for MKP-ref.

MKPC paste	Attribution	Chemical shift (ppm)	FWHM (ppm)	^{31}P fraction (%)
Before leaching	K-struvite ($MgKPO_4 \cdot 6H_2O$)	+6.5	0.7	76
	Residual KH_2PO_4	+4.1	1.0	1
	Broad hump *	+0.9	10.2	23

**This signal was not clearly assigned.*

The ^{31}P MAS-NMR spectrum of MKP-ref exhibited three different ^{31}P chemical environments (see top spectrum in Figure 3). The resonance at δ = +6.5 ppm was attributed to K-struvite (Gardner et al., 2015; Lahalle et al., 2018; Viani et al., 2017). A minor ^{31}P resonance at δ = +4.1 ppm (1% of the ^{31}P fraction) was attributed to residual KH_2PO_4, which was not detected by XRD due to its low content (Gardner et al., 2015; Lahalle et al., 2018). This indicates that KH_2PO_4 was not completely consumed after the 6-month curing period. The resonance at δ = +0.9 ppm could not be assigned with certainty. This resonance might correspond to one or several contributions of poorly crystallized phosphate phases, including *(i)* $Mg_2KH(PO_4)_2{\cdot}15H_2O$, (Lahalle et al., 2018; Xu et al., 2022), *(ii)* lünebergite ($Mg_3B_2(PO_4)_2(OH)_6{\cdot}6H_2O$) (Lahalle et al., 2018), *(iii)* an anhydrous, poorly crystallized orthophosphate $Mg_3(PO_4)_2$ (Viani et al., 2017), and/or *(iv)* hydrated magnesium phosphate phases ($Mg_3(PO_4)_2{\cdot}xH_2O$) (Kongshaug et al., 2001). In two recent papers, Viani et al., 2021, 2017 showed that hardening of a MKPC paste occurs through an amorphous-to-crystalline transformation, involving two distinct amorphous precursors of the final crystalline product (K-struvite), characterized by broad resonances at 3 ppm and 1.8 ppm. The authors suggested that, in analogy with the sol-gel processing of ceramics, the amorphous precursors may bear some structural motifs of K-struvite, the final crystalline phase.

3.2. Leaching tests: experimental results

3.2.1. Precipitate recovered from leachates

The leaching solution became visibly turbid upon immersion of paste samples, indicating the formation of a precipitate in the solution (Figure 4-a). Subsequently, after each renewal, solid and liquid phases were separated through centrifugation to isolate any precipitate that might have formed. During the first two renewals, the precipitate was easily recovered. From the third renewal onwards, the clarity of the leaching solutions improved over time. The recovered precipitate was rinsed with ethanol, dried at 38 °C for 24 h, and identified by XRD as hydroxyapatite (HAP) with low crystallinity (Figure 4-a).

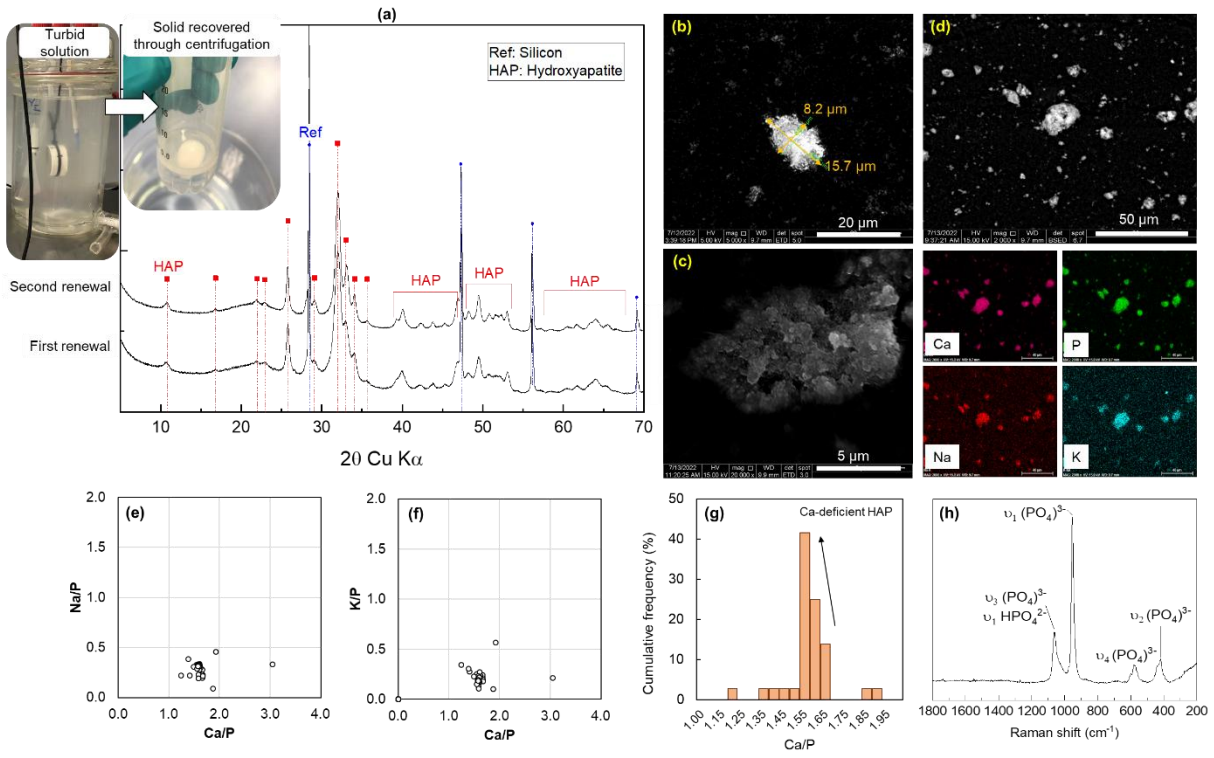

Figure 4 – Characterization of HAP **(a)** XRD patterns (range 5 °-70 ° 2θ), **(b)** SE image, **(c)** zoomed-in of an agglomerate of HAP crystals, **(d)** BSE image and EDS elemental mapping, **(e)** EDS semi-quantitative analyses Na/P vs. Ca/P, **(f)** K/P vs. Ca/P atomic ratios, **(g)** Distribution of Ca/P atomic ratios, and **(h)** Raman spectrum.

HAP particles, of approximatively 16 µm long and 8 µm wide, consisted of agglomerates of micrometer-sized crystals (Figure 4-b and c). EDS analyses showed the presence of Ca, P, Na and K in the HAP particles, which suggests the uptake of alkalis by HAP (Figure 4-d, e and f), as already observed by Stoll and Neuman, 1956. By suspending pure HAP in solutions containing KCl and NaCl at various concentrations, these authors observed indeed an uptake of Na, which was higher than that of K. Na ions entered the crystal surface of HAP by replacing Ca ions, whereas K ions remained in the hydration shell of HAP. The HAP particles obtained in the current study had a Ca/P ratio of 1.59±0.11 (arithmetic mean value with a confidence interval of 95 %) (Figure 4-g), suggesting the precipitation of Ca-deficient HAP (CDHA) (the Ca/P ratio of stoichiometric HAP is 1.67), possibly due to the uptake of Na.

Figure 4-h presents the Raman spectrum of the collected precipitate. The spectrum exhibited distinct bands, including the symmetric stretching mode (υ1) of phosphate at 960-962 cm^{-1}, which

corresponds to the tetrahedral $(PO_4)^{3-}$ group (P−O bond) typically reported in HAP (Penel et al., 1998; Wilson et al., 2005). The υ4 and υ2 bending modes (O−P−O bond) produced bands of weak intensity in the regions of 570–625 cm^{-1} and 400–490 cm^{-1}, respectively. The band at 1000-1095 cm^{-1} could be assigned to the υ3 $(PO_4)^{3-}$ domain (Penel et al., 1998), but also to the υ1 mode of hydrogen phosphate (HPO_4^{2-}) present in CDHA (Elliot, 1994; Wilson et al., 2005).

3.2.2. Leachates characterization

Figure 5 shows the evolution of the cumulative concentrations of K, Na, Ca, P, B, Si, S and Al in the leachates (in mmol/L) (i.e., total concentrations of soluble species measured in the leachates) and of pH as a function of the square root of time (in $days^{1/2}$). The Mg concentration always remained below the detection limit of the ICP-AES method (10 ppb). The red envelope represents the experimental analytical error. The subfigure in Figure 5-c plots the Ca concentration consumed from the initial solution. This means the difference between the Ca concentration measured in the leachates and the initial concentration in the leaching solution. Table 5 presents the initial composition of MKP-ref alongside with the cumulative leached element concentrations determined for each leaching period, expressed in mmol/g of paste. The leached fraction is presented as a percentage for each element, assuming an experimental paste density of 1,876.2 kg/m^3, which was obtained by total porosity accessible to water experiments.

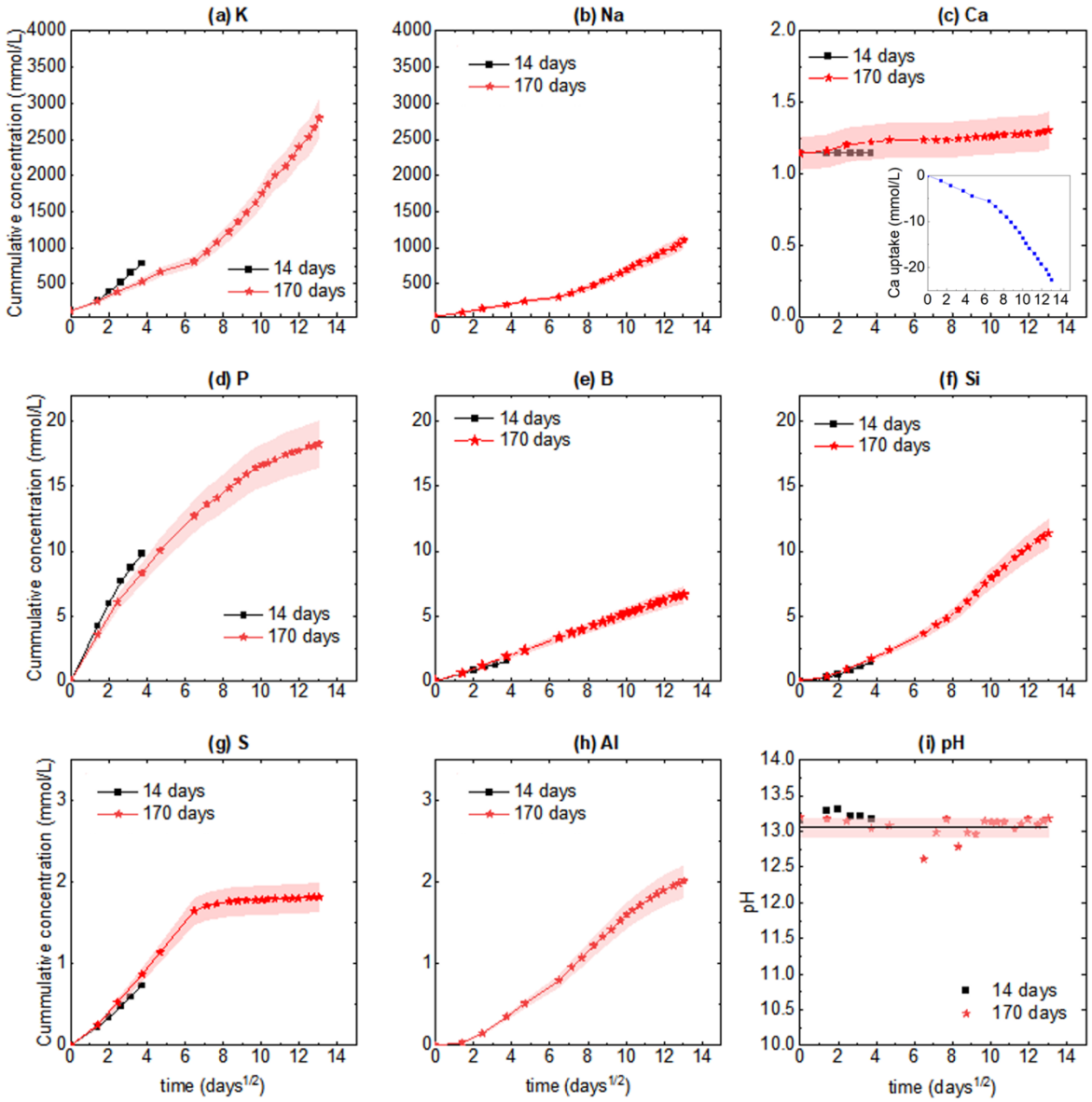

Figure 5 – Cumulative concentrations (in mmol/L) measured in the leachates as a function of the square root of time (days$^{1/2}$). **(a)** K, **(b)** Na, **(c)** Ca, **(d)** P, **(e)** B, **(f)** Si, **(g)** S, **(h)** Al, and **(i)** pH evolution. The analytical error is estimated to be 10 %.

Table 5 – Initial and leached elemental concentrations (given in mmol/g of MKPC paste) and pH values determined at 25 ºC.

			K	Na	Ca	Al	B	Fe	Mg	P	S	Si	pH
	days	Initial concentration	2.8	0.1	0.3	1.9	0.13	0.6	2.4	2.6	0.04	3.8	13.2±0.1
Leaching time	14	Leached concentration	-	-	-	0.01	0.03	0.0	0.0	0.2	0.02	0.03	13.2±0.1
		Leached fraction (%)	-	-	-	0.33	26.5	0.0	0.0	8.7	40.1	0.87	-
	170	Leached concentration	-	-	-	0.0	0.13	0.0	0.0	0.4	0.04	0.26	13.1±0.1
		Leached fraction (%)	-	-	-	2.4	100	0.0	0.0	16.3	100	6.91	-

K and Na leached concentrations are not presented as their quantification fell into the 10% error associated with the ICP-AES technique. Ca concentrations were below the ICP-AES detection limit.

The two leaching experiments provided rather well repeatable results. Soluble phosphates (excluding P that precipitated as CDHA) were released in the leachates, albeit at a decreasing rate over time. The cumulative concentration of B in the leachates increased linearly versus the square root of time, suggesting that its release was controlled by diffusion through the pore network of the cement paste. Mass balance calculations in Table 5 show that B may be depleted by the end of the 170-day leaching test. The leached Si, S, and Al resulted from dissolution of fly ash and/or impurities present in the raw materials. Si and Al cumulative concentrations exhibited similar evolution with time, while S was fully depleted after approximately 36 days of leaching. Unlike the other elements, calcium was significantly depleted from the leaching solution due to the precipitation of CDHA evidenced in section 3.2.1.

3.2.3. Characterization of leached solids

After leaching, paste samples presented thin white layers coating their exposed surfaces (Figure 6). The thickness of each sample was measured using a digital caliper with a measurement range of 0-25 mm and an accuracy of 0.001 mm. There was no observable interface retreat or expansion on the exposed surfaces of the leached solids. Despite the absence of any retreat or expansion, the exposed surfaces of the leached solids exhibited pronounced brittleness, and material deposited on these surfaces could be easily removed, especially after 170 days of leaching.

The Rainbow indicator was sprayed onto the cross-sections of the leached pastes. The color transformation from greenish to purple-blue indicated a rise in pH from 8, before leaching, to a value higher than 10.

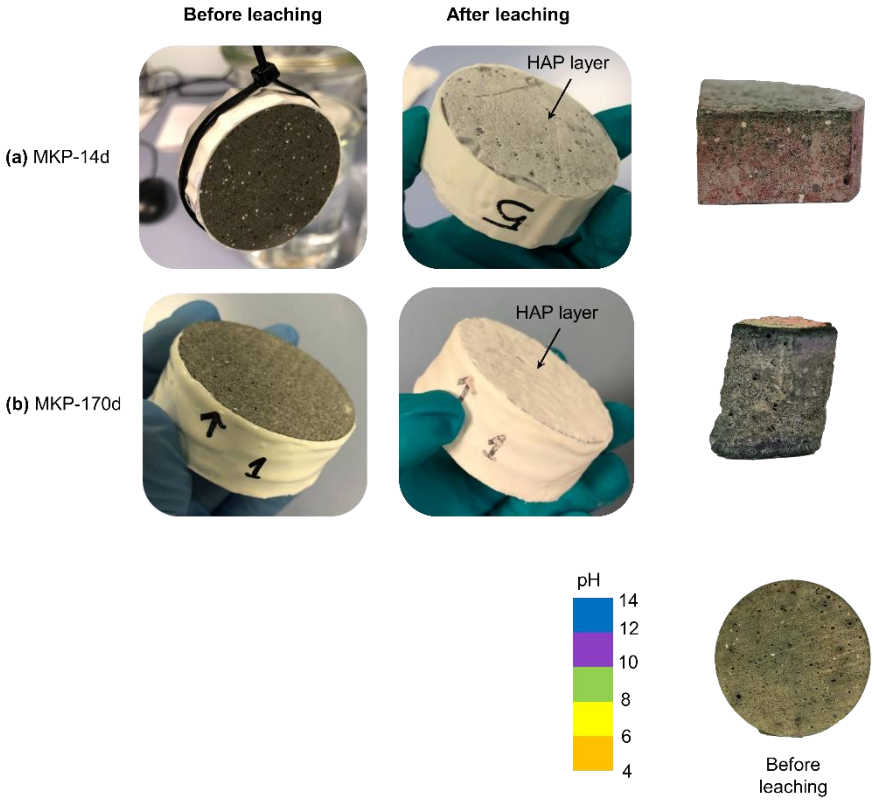

Figure 6 – Leached solids and estimation of pH using the Rainbow indicator **(a)** MKP-14d, and **(b)** MKP-170d.

3.2.3.1. SEM/EDS analyses and optical microscopy

The white layer observed on the exposed surfaces of the leached samples was enriched in Ca and P, suggesting the precipitation of a calcium phosphate phase such as hydroxyapatite (HAP). It measured approximately 12 ± 2 µm and 309 ±38 µm in MKP-14d and MKP-170d, respectively (Figure 7-a and b) and seemed very porous (Figure 7-c). Under this superficial layer, a degraded zone was evidenced by a darker grey color on the SEM/BSE images and a lighter gray by optical microscopy observations, indicating a smaller density than that of the sound material. EDS elemental mapping showed some areas enriched in magnesium, suggesting the precipitation of a Mg-containing phase which could

explain why Mg was not leached out of the sample (Figure 5 and Table 5). The elemental maps also showed a decrease in the P and K concentrations, which was consistent with the observed release of these species in the leachates.

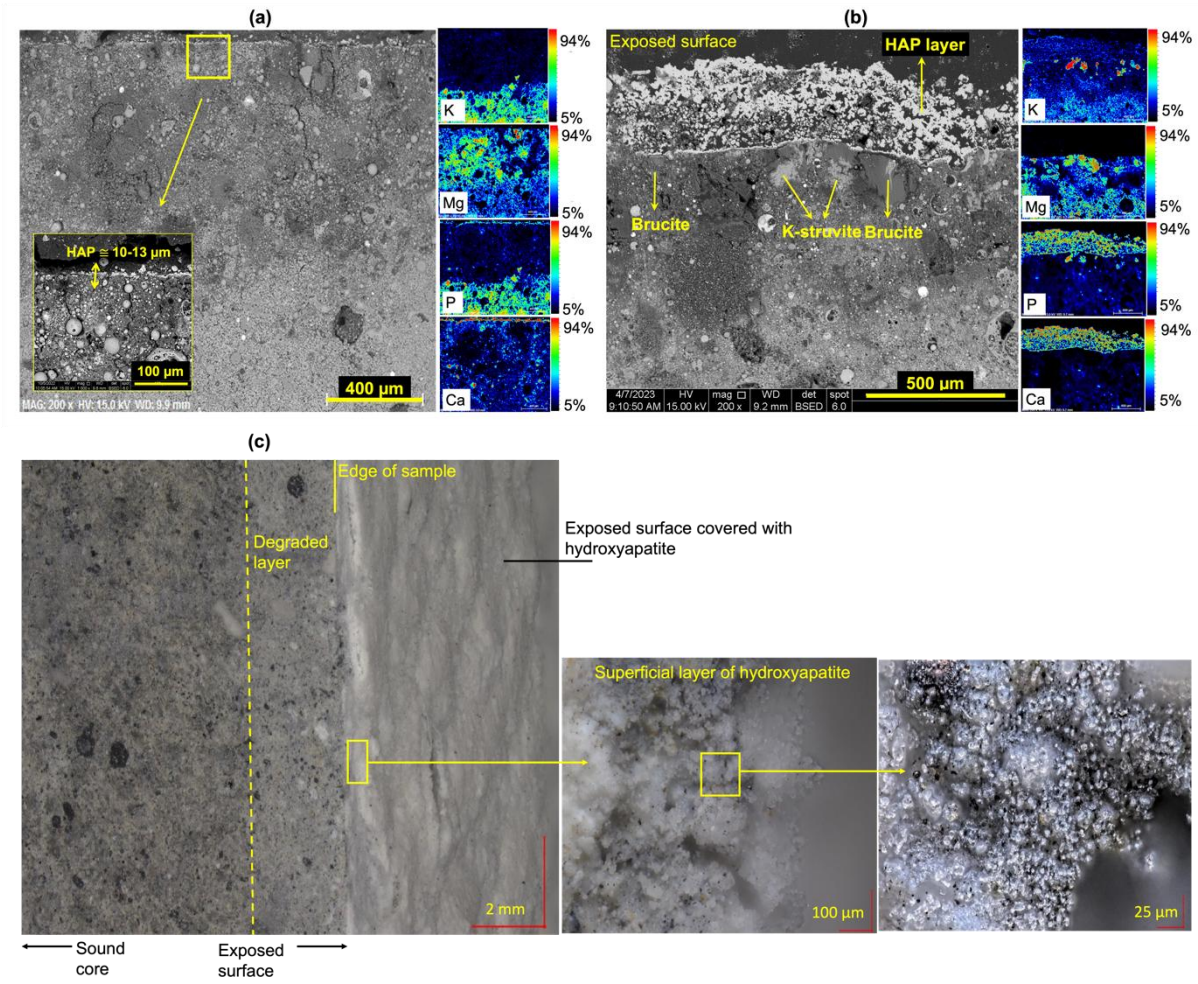

Figure 7 – Characterization of leached solids: SEM/EDS of **(a)** MKP-14d, and **(b)** MKP-170d. (c) Optical microscopy of MKP-170d.

Figure 8 presents the mixing diagrams of atomic ratios based on EDS analyses. The figure illustrates regions corresponding to various phases potentially present in the solids, including residual KH_2PO_4, K-struvite, $Mg_2KH(PO_4)_2{\cdot}15H_2O$, bobierrite ($Mg_3(PO_4)_2{\cdot}8H_2O$), cattiite ($Mg_3(PO_4)_2{\cdot}22H_2O$), phosphorrösslerite ($MgHPO_4{\cdot}7H_2O$), newberyite ($MgHPO_4{\cdot}3H_2O$), brucite ($Mg(OH)_2$), hydroxyapatite ($Ca_5(PO_4)_3(OH)$), and $CaK_3H(PO_4)_2$ (Lahalle et al., 2018; Lothenbach et al., 2019). Note that Ca-poor hydroxyapatite (CDHA) was not added in this figure as atomic ratios of Ca/P may vary, as shown in

Figure 4. Some additional phases were also included, such as magnesium hydrogen phosphate ($Mg(H_2PO_4)_2{\cdot}xH_2O$ or $MgH_2P_2O_7$), calcium silicate hydrate (C-S-H), and magnesium silicate hydrate (M-S-H) (Lahalle et al., 2018; Lothenbach et al., 2019; Xu et al., 2021, 2020). After leaching, EDS point analyses were primarily carried out from the surface to a depth of 2 mm.

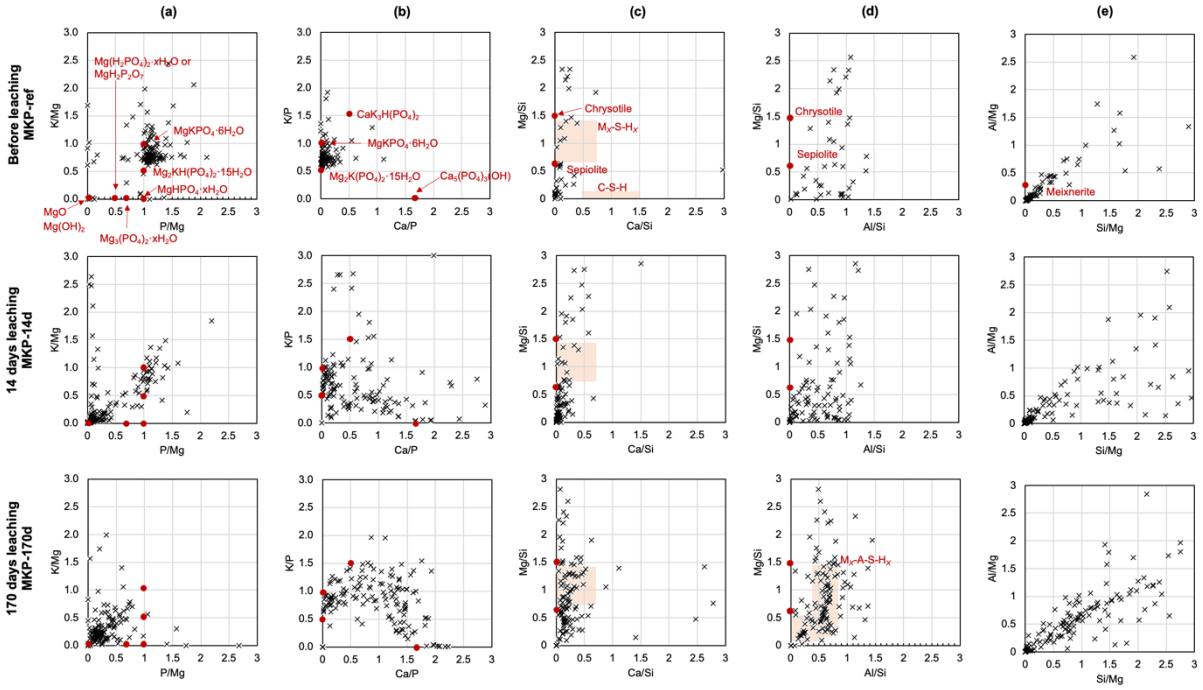

Figure 8 – EDS mixing diagrams of atomic ratios obtained from the MKPC paste samples before and after leaching (2 mm deep from the interface). **(a)** K/Mg *vs.* P/Mg, **(b)** K/P *vs.* Ca/P, **(c)** Mg/Si *vs.* Ca/Si, **(d)** Mg/Si *vs.* Al/Si, and **(e)** Al/Mg *vs.* Si/Mg.

The P/Mg and K/Mg ratios measured in the leached samples tended to decrease as compared to the pristine material, suggesting the dissolution of K struvite, and the possible precipitation of brucite. In MKP-14d sample, the P/Mg and K/Mg ratios were still comprised between those of K-struvite and $Mg_2KH(PO_4)_2{\cdot}15H_2O$ for a number of point analyses, indicating the persistence of K-struvite after leaching (Figure 8-a). In MKP-170d sample, the scatter plot was shifted towards origin, suggesting advanced dissolution of K-struvite and higher precipitation of brucite. The mixing diagrams plotting the K/P *vs.* Ca/P ratios (Figure 8-b) showed the precipitation of a Ca-phosphate phase, probably CDHA with a Ca/P ratio close to 1.5, or HAP possibly intermixed, at the submicronic level, with other phases having lower Ca/P ratio, such as $CaK_3H(PO_4)_2$. Additionally, both leached solids presented

EDS points with Mg/Si atomic ratios ranging from 0.7 to 1.4, which may correspond to the formation of Mg-silicates phases such as M_x-S-H_y, sepiolite ($Mg_4Si_6O_{15}(OH)_{12}\cdot 6H_2O$), or chrysotile ($Mg_3(Si_2O_5)(OH)_4$) (Figure 8-c). No EDS points were related to the formation of C-S-H.

In MKP-170d, some EDS point analyses indicated the formation of a compound with Al/Si atomic ratios varying from 0.2 to 0.6, suggesting the formation of Mg-silicate phases containing Al such as M_x-A_y-S-H_z (Figure 8-d). The incorporation of aluminum in both tetrahedral and octahedral sites of M-S-H phases having a Mg/Si ratio of 1.1 or 1.7 has been evidenced by Bernard et al., 2020. Nevertheless, the Al/Si ratio was limited to 0.15−0.18. Another possible explanation would be the intermixing of magnesium silicate phases with hydrotalcite-like phases, Al-phosphates (such as minyulite ($KAl_2(PO_4)_2OH\cdot 4H_2O$) or amorphous Al-phosphates) which have been predicted to form during hydration of MPC materials containing aluminates (Xu et al., 2022), or mullite ($Al_{4+2x}Si_{2-2x}O_{10-x}$, possibly containing up to 0.5 wt% MgO (Schneider et al., 2008)) supplied by the fly ash.

Finally, the Al/Mg *vs* Si/Mg mixing diagram evidenced a correlation between the Al and Si contents for a number of analysis points (Figure 8-e), likely corresponding to the glassy fraction of fly ash (Aughenbaugh et al., 2016). The Al/Si ratios in the pristine material and in the paste leached for 14 days were close to 1. Interestingly, this value decreased to about 0.67 in the sample leached for 170 days, suggesting that non-congruent dissolution of the glassy phase(s) occurred during the longer leaching test, with preferential release of Al compared to Si. It has already been reported that when fly ash is exposed to a strongly alkaline solution, Al is more prone to dissolve than Si due to weaker Al-O bonds than Si-O bonds (Li et al., 2011).

3.2.3.2. XRD analyses

Figure 9 displays some XRD patterns of powders obtained at different depths (denoted as “delta” on the y-axis) in MKP-14d and MKP-170d samples. The selected patterns are presented in the 5°-40° 2θ range to highlight the main differences. The crystalline phases and amorphous fraction in MKP-14d and MKP-170d samples were also quantified by Rietveld refinement (Table 6). Note that polycrystalline or low crystallinity nature of CDHA or HAP phases unable their quantification by

Rietveld refinement in the MKP-14d leached sample. Several minerals containing Mg, Al and/or Si were tested in the refinement of the XRD patterns of MKP-170d. Only meixnerite ($Mg_6Al_2(OH)_{18}\cdot 4H_2O$), a Mg-Al layered double hydroxide (LDH) phase with a structure close to hydrotalcite (Koritnig and Süsse, 1975), matched well the patterns.

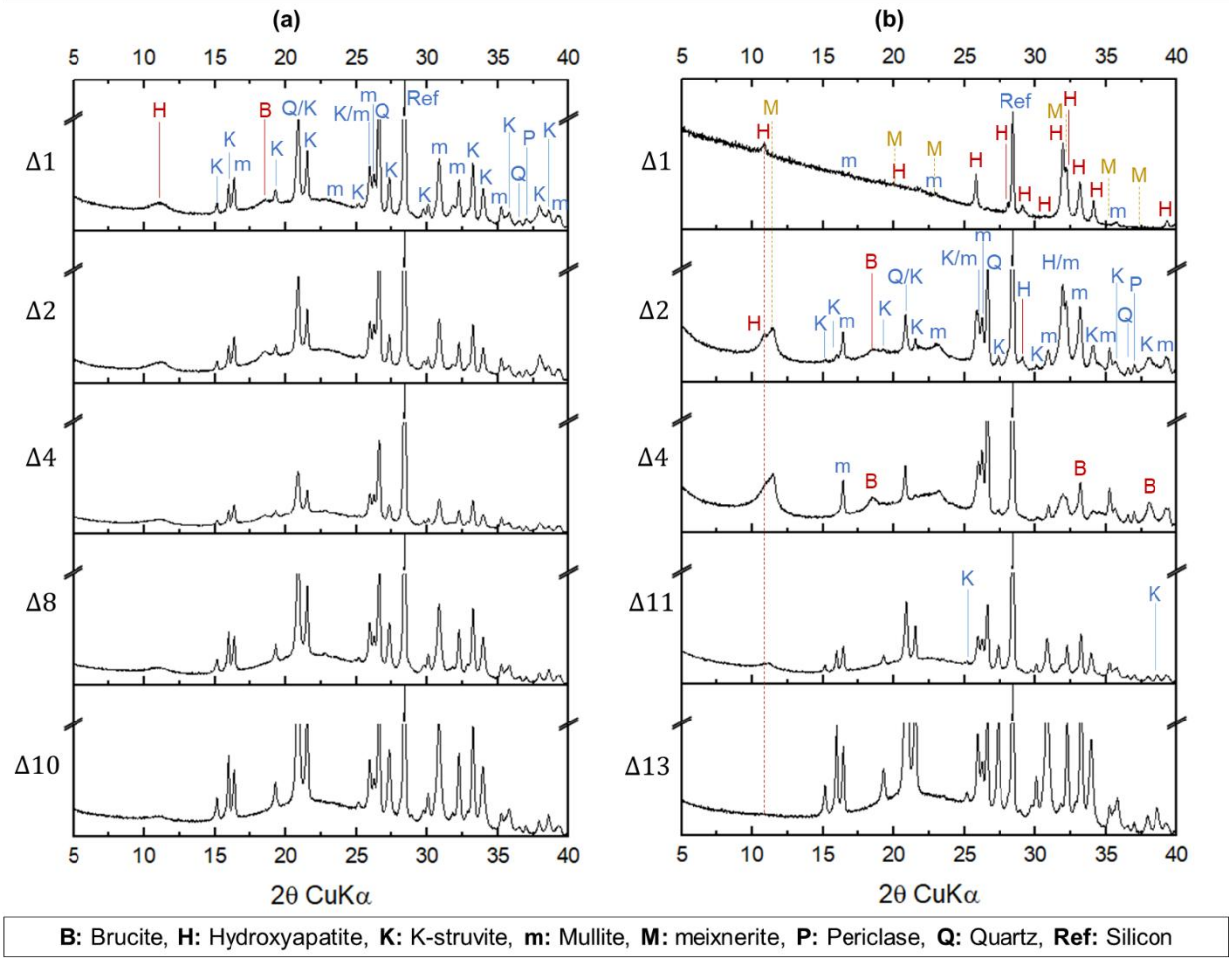

Figure 9 –XRD patterns obtained at different depths of **(a)** MKP-14d, and **(b)** MKP-170d. *Patterns are presented in the 5°-40° 2θ range to highlight the main differences. "Delta Δ" on the y-axis denotes the different depths where the samples were taken (cf. Table 6).*

Table 6 – Quantification of mineralogical phases in the leached solids using Rietveld refinement (results given in wt%).

	Depth (µm)	K-struvite	HAP[a]	Brucite	Mg-Al phase[b]	Amorphous	MgO	Quartz	Mullite

		Depth (µm)	K-struvite	HAP[a]	Brucite	Mg-Al phase[b]	Amorphous	MgO	Quartz	Mullite
MKP-ref		-	53.8	-	-	-	33.6	1.8	2.6	8.2
MKP-14d	Δ1	0 - 137	22.8	-	6.3	-	51.8	1.5	5.9	11.7
	Δ2	137 - 238	19.5	-	4.1	-	57.2	2.1	6.0	11.0
	Δ3	238 - 470	13.6	-	1.3	-	70.2	1.9	4.7	8.3
	Δ4	470 - 677	10.7	-	1.3	-	75.3	1.5	4.0	7.1
	Δ5	677 - 1009	10.3	-	0.6	-	81.0	1.0	2.6	4.6
	Δ6	1009 - 1387	16.9	-	0.0	-	72.3	1.4	3.4	6.1
	Δ7	1387 - 1878	31.2	-	0.0	-	52.5	2.3	4.7	9.2
	Δ8	1878 - 2439	39.0	-	0.0	-	42.2	2.2	5.8	10.7
	Δ9	2439 - 3000	32.3	-	0.0	-	54.0	1.3	4.2	8.2
	Δ10	3000 - 3648	48.5	-	0.0	-	33.8	2.5	5.5	9.6
MKP-170d	Δ1	0 - 579	0.0	51.0	0.0	0.0	49.0	0.0	0.0	0.0
	Δ2	579 - 854	7.6	26.1	10.7	9.4	27.6	2.7	4.8	11.1
	Δ3	854 - 1075	3.7	10.0	5.6	10.6	42.1	2.7	6.7	18.7
	Δ4	1075 - 1607	3.2	4.8	3.3	9.1	61.9	2.1	4.1	11.4
	Δ5	1607 - 1919	2.3	3.1	1.9	13.1	58.0	2.4	5.3	13.8
	Δ6	1919 - 2084	5.6	4.2	1.7	7.1	58.5	2.8	5.6	14.5
	Δ7	2084 - 2268	7.9	3.9	0.3	12.4	58.4	1.9	4.2	10.9
	Δ8	2268 - 2626	11.7	5.3	0.1	5.3	61.8	1.5	4.1	10.2
	Δ9	2626 - 3019	18.0	3.7	0.0	7.0	55.0	1.7	3.9	10.6
	Δ10	3019 - 3473	15.7	3.0	0.0	5.1	63.7	1.3	3.0	8.3
	Δ11	3473 - 3964	20.9	2.7	0.0	1.8	56.9	1.8	3.9	11.9
	Δ12	3964 - 4507	26.6	3.2	0.0	1.4	50.4	2.3	4.2	12.0
	Δ13	4507 - 8240	72.8	0.0	0.0	0.0	7.5	2.0	4.8	13.0

[a] *In the MKP-14d powders, quantification by Rietveld refinement of CDHA or HAP phases was not possible due to their polycrystalline or low crystallinity nature.*
[b] *Mg-Al layered double hydroxide (LDH) phase with a structure close to hydrotalcite.*

K-struvite was detected in all the patterns of MKP-14d but was absent from the first layer (Δ1: 0-579 µm) of MKP-170d (Figure 9-b). Its content in the deepest investigated layer of MKP-14 d was close to that of the pristine material. In MKP-170d, however, it was significantly higher (72.8 wt% *vs* 53.8 wt% in MKP-ref), indicating a progress of cement hydration during the leaching test, with the conversion of amorphous precursors into more crystalline K-struvite. The periclase/mullite and periclase/quartz weight ratios remained approximatively constant (Table 6), except in the first layer. Since mullite and quartz are non-reactive phases, this result shows that the consumption of MgO was almost negligible during the leaching tests. The residual MgO likely corresponded to large particles having very low reactivity.

Leaching caused the precipitation of novel crystalline phases. XRD confirmed the precipitation of hydroxyapatite (Figure 9-a) with low crystallinity (broad peak at 10°-12° 2θ) near the exposed surface of the leached cement pastes, but also deeper in the materials. In MKP-170d, this peak seemed to shift towards higher angles, possibly due to the presence of meixnerite ($Mg_6Al_2(OH)_{18}\cdot 4H_2O$), which was identified up to a depth of 4.5 mm. Its amount varied between 1.4 wt% (Δ1) to 13.1 w% (Δ5). Moreover, brucite ($Mg(OH)_2$) precipitated in both leached solids, up to a depth of about 1 mm in MKP-14d, and 2.6 mm in MKP-1710d. Finally, precipitation of low Ca/P calcium phosphates such as $CaK_3H(PO_4)_2$, hydrated magnesium silicate phases or phospho-aluminate phases such as OH-minyulite ($KAl_2(PO_4)_2OH\cdot 4H_2O$) was not evidenced by XRD.

3.2.3.3. ^{31}P MAS-NMR analyses

The precipitate recovered from the leachates (section 3.2.1) and some samples collected at various depths in the leached cement pastes were analyzed by ^{31}P MAS-NMR, meaning that only the fraction of ^{31}P was quantified (Figure 3 and Table 7).

Table 7 - ^{31}P site fractions (mol. %) assessed from decomposition of ^{31}P MAS-NMR spectra after leaching.

		Depth (µm)	Phase[a]	Chemical shift (ppm)	FWHM (ppm)	^{31}P fraction (%)
14-day leached solid	Δ1	0 - 137	K-struvite	+6.3	1.6	69
			HAP	+2.6	2.7	31
	Δ2	137 - 238	K-struvite	+6.2	1.6	60
			HAP	+2.6	2.7	40
	Δ8	1387 - 1878	K-struvite	+6.3	1.7	91
			HAP	+2.5	3.6	9
170-day leached solid	Δ1	0 - 579	K-struvite[b]	+5.3	2.3	12
			HAP	+2.7	2.3	88
	Δ2	579 - 854	K-struvite[b]	+6.0	2.1	15
			HAP	+2.6	2.6	85
	Δ3	854 - 1075	K-struvite[b]	+5.9	2.1	12
			HAP	+2.5	2.8	88
	Δ4	1075 – 1607	K-struvite[b]	+6.0	2.4	15
			HAP	+2.6	3.0	85
	Δ5	1607 - 1919	K-struvite	+6.2	2.5	24
			HAP	+2.6	3.2	76
	Δ6	1919 - 2084	K-struvite	+6.2	2.1	31
			HAP	+2.6	3.2	70

[a] *The fraction of ^{31}P was estimated to be present in either K-struvite or HAP (±0.2%).*

[b] *K-struvite probably disordered or presenting structural defaults.*

The precipitate formed in the leachates showed a single ^{31}P resonance at δ = +3.0 ppm (Figure 3), which was consistent with the chemical shift reported for stoichiometric HAP (Ca/P of 1.67) and for CDHA (Elliot, 1994). The spectra from the leached samples showed two main resonances at $\delta \approx$ +6.2 ppm and $\delta \approx$ +2.6 ppm, which could be assigned to K-struvite and HAP/CDHA respectively. There was no evidence for the presence of OH-minyulite ($KAl_2(PO_4)_2(OH)\cdot 4H_2O$) and $CaK_3H(PO_4)_2$, whose signals are expected at δ = -9.6 ppm and δ = 0 ppm, respectively (Dick et al., 1998; Xu et al., 2020). In sample MKP-170d, the spectrum of the powder collected in the first layer close to the exposed surface (Δ_1), presented a peak centered at δ = 5.3 ppm, significantly shifted as compared to that of crystalline K-struvite ($\delta \approx$ +6.2 ppm). This shift of position indicated a change in the P environment, possibly resulting from the amorphization of K-struvite (this mineral was not detected by XRD in Δ_1 sample), or its transformation into another amorphous or poorly crystallized phase (e.g., hazenite $Mg_2NaK(PO_4)_2.14H_2O$).

In the 14-day leached solid, quantification presented in Table 7 showed a significant increase in the ^{31}P fraction in HAP in the layer close to the surface. In layer Δ_8, 91% of ^{31}P was estimated to be present in the form of K-struvite, which can be crystalline or nano-crystalline/amorphous, while 9% of the ^{31}P was estimated to be in HAP. This may indicate less degradation of the sample in deeper layers. It is important to note that this fraction of ^{31}P should not be confused with the total amount of K-struvite present in the sample. As indicated in Table 6, XRD analyses estimated that only 39% of the sample was composed of crystalline K-struvite, an amount lower than that of the original sample (i.e., before leaching). In the 170-day leached solid, the proportion of ^{31}P significantly decreased in K-struvite, while its proportion increased in HAP, indicating a higher level of degradation in this sample.

3.3. Modeling results

3.3.1. Input data

The composition of MKP-ref was simplified for modeling (Table 3). K-struvite was assumed to be the main hydration product. Its content was inferred from XRD and Rietveld analyses. Therefore, the volume fractions of residual MgO and fly ash were considered, although these components were

506 treated as inert. In addition, traces of hazenite (≈2x10^{-11} mmol/L), predicted to be thermodynamically
507 stable, were also included in the initial matrix composition. The initial porosity of the paste was set at
508 its experimental value of 15.5% (as determined by total porosity accessible to water) and assumed to
509 be fully saturated. The pore solution, extracted using pressure from MKP-ref after 6 months of curing,
510 presented a pH of about 8.0 (at 25 ºC) and mainly comprised potassium (1033.8 mmol/L), magnesium
511 (1.1 mmol/L), phosphate (370 mmol/L), sodium (13.2 mmol/L) and borate (136.4 mmol/L) ions. Note
512 that this solution was still oversaturated with respect to K-struvite (Saturation Index of 0.87).

513 **Table 8 –** Main parameters defining the initial composition of the MKPC paste in the model. Concentrations are
514 given in mmol/L of interstitial solution.

$MgKPO_4 \cdot 6H_2O$	KH_2PO_4	$B(OH)_3$	K_2O	Na_2O
20700	565	135	237	50

515 **Na_2O was added to adjust the initial pH at 8.0. Na_2O and K_2O are fictive species which fully dissolve, thus*
516 *providing Na^+, K^+ and OH^- ions to the pore solution.*
517

518 *3.3.2. Phase evolution in the leached cement paste*

519 Figure 10 displays the phase evolution, predicted by modeling, in the paste after 14 and 170 days of
520 leaching. The effective diffusion coefficient (D_e) in the cement paste was adjusted at 1.37x10^{-13} m^2/s to
521 reproduce the experimental precipitation front of brucite in the sample leached for 14 d.
522 Modeling showed that dissolution of K-struvite occurred, producing an increase in porosity and
523 effective diffusion coefficient (Figure 10-b and d). This was accompanied by the precipitation of
524 brucite and hydroxyapatite (HAP) near the exposed surface, along with traces of hazenite. Note that
525 the precipitation of HAP was predicted to occur only close to the exposed surface, whereas
526 experimentally it was observed deeper in the material and coexisted with brucite and K-struvite. The
527 extent of K-struvite dissolution was predicted in both pastes leached for 14 d and 170 d. Nonetheless,
528 the thickness of the zone where brucite precipitated was underestimated by the model in MKP-170d.
529 HAP and brucite were also predicted to precipitate in the leaching solution. HAP precipitation in
530 solution was in line with experimental results (cf. Figure 4). Nonetheless, brucite was not detected
531 experimentally possibly due to the low concentrations. Moreover, the model predicted the gradual

increase in pH from 8 in the sound core to 13 at the leached surface. Besides, modeling tended to overestimate Ca concentrations and to underestimate P and B concentrations in solution.

Several hypotheses could be postulated to explain the differences between the experimental and modeling results: (i) the paste composition was oversimplified in the model due to a lack of thermodynamic data of phosphate phases available in the literature. In this model, only the aqueous fraction of B was taken into account, whereas Lahalle et al., 2018 have shown that boron is also partly precipitated as a boro-phosphate phase. Nevertheless, the composition of this phase is still unknown, as well as its thermodynamical properties, and thus it could not be included in the model. Consequently, the model predicted a too fast depletion of B from the cement paste and underestimated its total concentration released in solution. (ii) The solubility of HAP was overestimated. Thus, precipitation of HAP occurred only very close to the surface. It should be noted that there is a rather wide range of thermodynamic data reported for synthetic HAP (Vieillard and Tardy, 1984), and thus, the extent of precipitation of HAP depends on the selected value. (iii) The model predicted the precipitation of traces of hazenite ($Mg_2NaK(PO_4)_2.14H_2O$) in the leached solid. Hazenite concentrations were however too low (ranging from $2x10^{-11}$ to $1x10^{-4}$ mmol/L of paste) to be detected experimentally. Hazenite has been reported as a degradation product of K-struvite at pH >7 by several authors (Lahalle et al., 2019; Xu et al., 2023), but is very difficult to evidence in cement pastes. Its crystal structure corresponds to a superstructure of K- and Na-struvite (Yang et al., 2014, 2011; Yang and Sun, 2004) and thus possesses many structural features similar to those of K-struvite. Lahalle et al., 2019 observed by SEM/EDS some sodium enrichment, and thus potentially the presence of hazenite, in cement pastes exposed to a synthetic PC pore solution. Xu et al., 2023 succeeded in evidencing by XRD the precipitation of small amounts of hazenite when synthetic K-struvite was exposed to an alkaline solution, but failed to detect this phase when a cement paste was used.

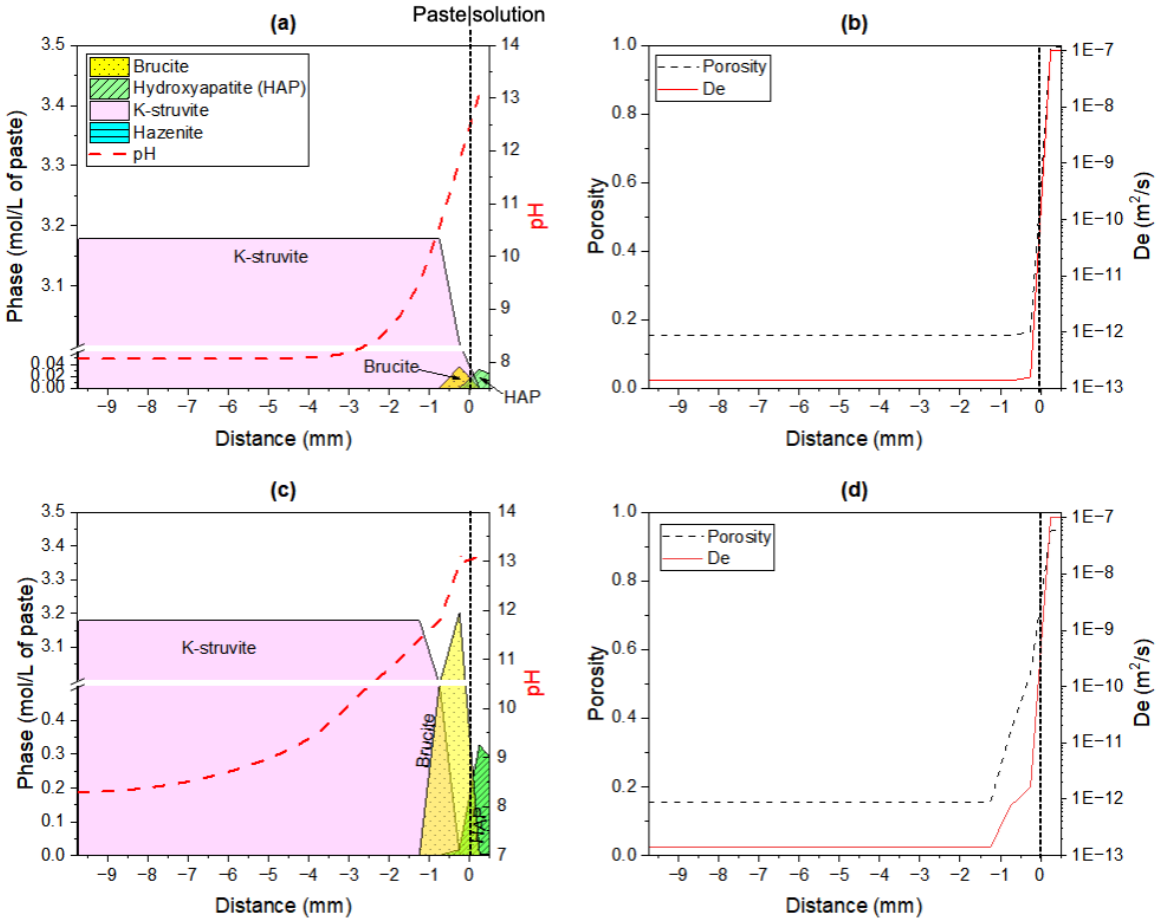

Figure 10 – Predicted evolution of the cement pastes: mineral phases and pH evolution, porosity, and effective diffusion coefficient (De) at **(a), (b)** 14 days, and **(c), (d)** at 170 days of leaching. *Traces of hazenite precipitated all along the paste (ranging from* $\approx 2\times10^{-11}$ *to* $\approx 1\times10^{-4}$ *mmol/L). Black dotted line indicates the paste-solution interface.*

4. Discussion

The findings of this study highlight the complex degradation process of MKPC paste samples under aggressive alkaline conditions. A phase evolution was observed near the leached surface, leading to the dissolution of K-struvite. In these samples, no interface retreat was observed since novel phases precipitated, which differs from what was observed by Diaz Caselles et al., 2024 on MKPC paste samples leached by demineralized water. Under alkaline conditions, the formation of calcium-deficient hydroxyapatite (CDHA) resulted from the reaction between Ca^{2+} ions present in the leaching solution, and phosphate anions provided by the MKPC paste (initially dissolved in the pore solution or released

568 by the dissolution of phosphate minerals such as K-struvite, residual KH_2PO_4 and/or other amorphous
569 phosphate phases evidenced in the pristine material). A layer formed at the solid/solution interface,
570 and its thickness increased with the leaching time (≈12 µm at 14 days, and ≈300 µm at 170 days).
571 Even though hydroxyapatite (HAP) is a mineral known for its low solubility (Elliot, 1994), its
572 formation was not sufficient to ensure the long-term durability of the MKPC pastes. The superficial
573 layer was rather porous (as evidenced by SEM/EDS in Figure 7) and did not seem to play any
574 protective role, since degradation progressed significantly between 14 days and 170 days of leaching.
575 More diffuse precipitation of poorly crystallized HAP was also evidenced by XRD under this surface
576 layer, up to a depth of ≈4 mm in the sample leached for 170 days. SEM/EDS analyses suggested the
577 precipitation of CDHA, since the Ca/P ratio was inferior to 1.67, the expected value for HAP, for a
578 large number of point analyses. Nevertheless, the additional formation of amorphous calcium
579 phosphate (ACP) cannot be excluded. ACP often occurs as a transient phase during the formation of
580 non-stoichiometric hydroxyapatite in aqueous systems (Boskey and Posner, 1973; Chow, 1999; Elliot,
581 1994; Zhang et al., 2011). When it is prepared by rapid precipitation in the pH range 8.9 – 11.7, its
582 Ca/P molar ratio is close to 1.5 (Combes and Rey, 2010; Heughebaert and Montel, 1977). Chemical
583 shifts ranging from 1.7 to 3.0 ppm have been reported for ACP analyzed by ^{31}P MAS-NMR (Belton et
584 al., 1988; Roufosse et al., 1984; Tropp et al., 1983). These values are close to those obtained for HAP,
585 making the two calcium phosphates difficult to distinguish on the ^{31}P spectra based on this sole
586 parameter. It should be noted that no calcium phosphate phases were detected on MKPC samples
587 leached under neutral conditions, as reported in Diaz Caselles et al., 2024. This can be attributed to the
588 absence of Ca^{2+} ions in the demineralized water.
589 Magnesium dissolved from the cement phases almost entirely reprecipitated in the cement matrix.
590 Two main phases formed, brucite, and an hydrotalcite-like phase, which may be meixnerite
591 ($Mg_6Al_2(OH)_{18}.4H_2O$) according to its diffraction pattern (cf. Figure 9). Precipitation of this
592 magnesium aluminate hydrate implied that the glassy fraction of the fly ash partly dissolved, since it
593 was the only source of aluminate in the system. Such reactivity of the fly ash was also indicated by the
594 decrease in its Al/Si content, as highlighted by EDS analyses (Figure 8-e). It was enhanced by the pH
595 increase of the pore solution occurring in the leached sample (Kumar et al., 2020; Wang et al., 2020).

Modeling showed indeed a pH gradient from 8 (initial pH of the pore solution) to 13, and experimental observations using a pH indicator confirmed that the pH exceeded 10 in the leached solid (cf. Figure 6 and Figure 10). The mixing diagrams, built from the EDS point analyses in the degraded part of the cement paste, also suggested the precipitation of magnesium silicate phases, with Mg/Si atomic ratios ranging from 0.7 to 1.4, and possibly containing aluminate (Figure 8). These phases were not detected by XRD, which means that they were amorphous or poorly crystalline. Previous studies have also reported the presence of M-S-H upon hydration of MKP cement (Xu et al., 2021, 2020). M-S-H have an ill-defined layered structure similar to that of hydrated precursors of 2:1 and 1:1 phyllosilicates (Bernard et al., 2019a; Nied et al., 2016; Roosz et al., 2015). Their stoichiometry may vary, with a Mg/Si molar ratio typically comprised between 0.7 and 1.5 (Nied et al., 2016). At Mg/Si ≥ 1.3, M-S-H coexist with brucite. They can also incorporate aluminum in their structure, in both tetrahedral and octahedral sites (Bernard et al., 2020). Some studies have reported that M-S-H are stable at pH values ranging from 9 to 11 (Nied et al., 2016) or from 8 to 14 (Bernard et al., 2019b). Therefore, it would be interesting to estimate the zone of occurrence of M-S-H in the leached samples. The poor crystallinity of M-(A)-S-H makes their characterization by XRD a difficult task (Roosz et al., 2015). It was attempted to highlight their presence by ^{29}Si MAS NMR. However, the collected spectra (not presented here) were complex due to signals overlapping and did not enable to confirm or infirm their formation. It is worth noting that Diaz Caselles et al., 2024 found that leaching MKPC samples (with fly ash as a filler) under neutral conditions did not activate the fly ash, and consequently, no novel phases containing Al or Si were observed after leaching.

The phase evolution induced by leaching of MKPC pastes under alkaline condition influenced the mechanical properties of the cement paste. The superficial layer, mainly consisting of HAP was rather porous and brittle. The subsequent layer, containing brucite, was also abraded rather easily whereas, at higher depth, the paste appeared much more resistant. These qualitative observations are consistent with the calculations carried out with the reactive transport model, which show that, going from the sound core to the leached surface, porosity starts to increase when brucite precipitates (Figure 10). This suggests that brucite may be regarded as a good indicator of MKPC paste alteration from a mechanical point of view: its presence would indicate a degraded zone with low mechanical strength.

The findings in this investigation may suggest approaches to enhance the durability of MKPC materials, consistent with Diaz Caselles et al., 2024:

- Increasing the Mg/P molar ratio of the cement. This would result in less depletion of KH_2PO_4 and fewer available P ions for precipitation as calcium phosphates.
- Utilizing a filler other than fly ash. This would enable modification of the paste microstructure and, consequently, its transport properties. A change in filler could ensure a lower diffusion coefficient and reduced porosity.

5. Conclusion

This study aimed to *(i)* investigate the leaching behavior of MKPC paste samples (with fly ash a filler) under alkaline condition, and *(ii)* gain insights into their degradation mechanisms. To this end, semi-dynamic leaching tests were conducted on MKPC paste monoliths using an alkaline solution (pH 13.2±0.1), which simulated a simplified pore solution of a conventional concrete that may be encountered close to the MKPC-based material. The leaching solution was renewed over time and the leachates were analyzed. The mineralogy and microstructure of the leached cement pastes were also characterized at the end of the leaching tests. The main conclusions drawn from this work are as follows:

1. Leaching by the alkaline solution modified the phase assemblage in the cement paste near the exposed surface. K-struvite tended to dissolve while Ca-deficient hydroxyapatite (CDHA), brucite and an hydrotalcite-like phase (possibly meixnerite $Mg_6Al_2(OH)_{18}.4H_2O$) precipitated. The additional formation of other phases such as M-(A)-S-H, amorphous calcium phosphate (ACP) and hazenite was possible, but still needs to be confirmed.
2. The leached solids did not exhibit any interface retreat. However, the exposed surfaces of the leached solids were highly brittle, and material was easily removed by scratching.
3. A layer of CDHA rapidly formed on the exposed surfaces and its thickness increased with the leaching duration. However, it was not sufficient to clog the porosity and protect the samples from further degradation, as the alterations fronts were found to be greater and more detrimental in the

170-day leached solid than in the 14-day leached solid. After 170 days of leaching, the altered layer had a thickness of about 4.5 mm.

4. The glassy fraction of the fly ash used as a filler in the paste formulation was shown to partly react due to the pH increase occurring close to the leached surface.
5. A reactive transport model was used to simulate the leaching experiments. Despite the simplified composition of the paste used for the calculations, the main phase evolutions (dissolution of K-struvite, and precipitation of both brucite and hydroxyapatite) were well predicted by the model.
6. To improve modeling, future work should consider the determination of solubility products of boro-phosphate phases lacking in the literature to use a more realistic paste composition. The glassy fraction of fly ash should be considered as reactive to enable the formation of phases containing aluminates and/or silicates. Finally, it would be necessary to measure experimentally the diffusion coefficient D_e in pristine and altered MKPC pastes to avoid adjusting this parameter in the model.

Credit authorship statement

Laura Diaz Caselles: Investigation, Methodology, Software, Writing – Original Draft, Project administration. **Céline Cau Dit Coumes:** Conceptualization, Validation, Writing – review and editing, Supervision, Funding acquisition, Project administration. **Pascal Antonucci:** Sample fabrication, Experimental setup. **Angélique Rousselet:** Conceptualization, Validation, Writing – review and editing. **Adel Mesbah:** Conceptualization, Data analysis, Writing – review and editing. **Valérie Montouillout:** Conceptualization, Data analysis, Writing – review and editing.

Declaration of competing interest

The authors declare no conflict of interest.

Data availability

Data will be made available on request.

Acknowledgements

This project has received funding from the European Union's Horizon 2020 research and innovation programme for Nuclear Fission and Radiation Protection Research (Call NFRP-2019-2020) under grant agreement No. 945098 (PREDIS).

Many thanks are given to Laurent De Windt for the assistance with HYTEC modeling.

References

Adenot, F., Buil, M., 1992. Modelling of the corrosion of the cement paste by deionized water. Cement and Concrete research 22, 489–496.

Arora, A., Singh, B., Kaur, P., 2019. Novel material i.e. Magnesium phosphate cement (MPC) as repairing material in roads and buildings. Materials Today: Proceedings 17, 70–76. https://doi.org/10.1016/j.matpr.2019.06.402

Aughenbaugh, K.L., Stutzman, P., Juenger, M.C.G., 2016. Identifying Glass Compositions in Fly Ash. Frontiers in Materials 3. https://doi.org/10.3389/fmats.2016.00001

Belton, P.S., Harris, R.K., Wilkes, P.J., 1988. Solid-state phosphorus-31 NMR studies of synthetic inorganic calcium phosphates. Journal of Physics and Chemistry of Solids 49, 21–27. https://doi.org/10.1016/0022-3697(88)90129-1

Bernard, E., Lothenbach, B., Cau-Dit-Coumes, C., Pochard, I., Rentsch, D., 2020. Aluminum incorporation into magnesium silicate hydrate (M-S-H). Cement and Concrete Research 128, 105931. https://doi.org/10.1016/j.cemconres.2019.105931

Bernard, E., Lothenbach, B., Chlique, C., Wyrzykowski, M., Dauzères, A., Pochard, I., Cau-Dit-Coumes, C., 2019a. Characterization of magnesium silicate hydrate (M-S-H). Cement and Concrete Research 116, 309–330. https://doi.org/10.1016/j.cemconres.2018.09.007

Bernard, E., Lothenbach, B., Pochard, I., Cau- Dit- Coumes, C., 2019b. Alkali binding by magnesium

699 silicate hydrates. Journal of the American Ceramic Society 102, 6322–6336.
700 https://doi.org/10.1111/jace.16494

701 Boskey, A.L., Posner, A.S., 1973. Conversion of amorphous calcium phosphate to microcrystalline
702 hydroxyapatite. A pH-dependent, solution-mediated, solid-solid conversion. The Journal of
703 Physical Chemistry 77, 2313–2317. https://doi.org/10.1021/j100638a011

704 Braney, M.C., Haworth, A., Jefferies, N.L., Smith, A.C., 1993. A study of the effects of an alkaline
705 plume from a cementitious repository on geological materials. Journal of Contaminant
706 Hydrology 13, 379–402. https://doi.org/10.1016/0169-7722(93)90072-Z

707 Buj, I., Torras, J., Rovira, M., de Pablo, J., 2010. Leaching behaviour of magnesium phosphate
708 cements containing high quantities of heavy metals. Journal of Hazardous Materials 175, 789–
709 794. https://doi.org/10.1016/j.jhazmat.2009.10.077

710 Cau Dit Coumes, C., Lambertin, D., Lahalle, H., Antonucci, P., Cannes, C., Delpech, S., 2014.
711 Selection of a mineral binder with potentialities for the stabilization/solidification of aluminum
712 metal. Journal of Nuclear Materials 453, 31–40. https://doi.org/10.1016/j.jnucmat.2014.06.032

713 Chau, C.K., Qiao, F., Li, Z., 2012. Potentiometric Study of the Formation of Magnesium Potassium
714 Phosphate Hexahydrate. Journal of Materials in Civil Engineering 24, 586–591.
715 https://doi.org/10.1061/(ASCE)MT.1943-5533.0000410

716 Chow, L.C., 1999. Calcium Phosphate Cements: Chemistry, Properties, and Applications. MRS
717 Proceedings 599, 27. https://doi.org/10.1557/PROC-599-27

718 Combes, C., Rey, C., 2010. Amorphous calcium phosphates: Synthesis, properties and uses in
719 biomaterials. Acta Biomaterialia 6, 3362–3378. https://doi.org/10.1016/j.actbio.2010.02.017

720 De Windt, L., Badreddine, R., 2007. Modelling of long-term dynamic leaching tests applied to
721 solidified/stabilised waste. Waste Management 27, 1638–1647.
722 https://doi.org/10.1016/j.wasman.2006.07.019

De Windt, L., Devillers, P., 2010. Modeling the degradation of Portland cement pastes by biogenic organic acids. Cement and Concrete Research 40, 1165–1174. https://doi.org/10.1016/j.cemconres.2010.03.005

Diaz Caselles, L., Cau Dit Coumes, C., Antonucci, P., Rousselet, A., Mesbah, A., Montouillout, V., 2024. Chemical degradation of magnesium potassium phosphate cement pastes during leaching by demineralized water: Experimental investigation and modeling. Cement and Concrete Research 178, 107456. https://doi.org/10.1016/j.cemconres.2024.107456

Dick, S., Grossmann, G., Ohms, G., Zeiske, T., 1998. ChemInform Abstract: Aluminum Phosphates with Non- Centrosymmetric Layer- and Framework- Structures of Topologically Related Motifs. Part 1. KAl2 (PO4)2 (OH)×4H2O. ChemInform 29. https://doi.org/10.1002/chin.199814010

Ding, Z., Dong, B., Xing, F., Han, N., Li, Z., 2012. Cementing mechanism of potassium phosphate based magnesium phosphate cement. Ceramics International 38, 6281–6288. https://doi.org/10.1016/j.ceramint.2012.04.083

Elliot, J.C., 1994. Structure and Chemistry of the Apatites and Other Calcium Orthophosphates, Department of Child Dental Health The London Hospital Medical College Turner Street London El 2AD, U.K. Elsevier, Amsterdam. https://doi.org/10.1021/ja945007t

Frontera, C., Rodríguez-Carvajal, J., 2003. FullProf as a new tool for flipping ratio analysis. Physica B: Condensed Matter 335, 219–222. https://doi.org/10.1016/S0921-4526(03)00241-2

Gardner, L.J., Bernal, S.A., Walling, S.A., Corkhill, C.L., Provis, J.L., Hyatt, N.C., 2015. Characterisation of magnesium potassium phosphate cements blended with fly ash and ground granulated blast furnace slag. Cement and Concrete Research 74, 78–87. https://doi.org/10.1016/j.cemconres.2015.01.015

Heughebaert, J.-C., Montel, G., 1977. Étude de l'évolution de l'orthophosphate tricalcique non

747 cristallin en phosphate apatitique à la faveur d'une réaction chimique, à température ordinaire.
748 Revue de Physique Appliquée 12, 691–694.
749 https://doi.org/10.1051/rphysap:01977001205069100

750 Ionascu, L., Nicu, M., Turcanu, C., Dragolici, F., Rotarescu, G.H., 2014. Study of the conditioning
751 matrices for aluminium radioactive wastes. Romanian Journal of Physics 59, 360–368.

752 Janot, C., Ilschner, B., 2001. Biocéramiques et biociments résorbables pour le comblement osseux, in:
753 PPUR (Ed.), Traité Des Matériaux. p. 415.

754 Kongshaug, K.O., Fjellvåg, H., Lillerud, K.P., 2001. The synthesis and crystal structure of a hydrated
755 magnesium phosphate Mg3(PO4)2·4H2O. Solid State Sciences 3, 353–359.
756 https://doi.org/10.1016/S1293-2558(00)01109-2

757 Koritnig, S., Süsse, P., 1975. Meixnerit, Mg6Al2(OH)18·4H2O, ein neues Magnesium-Aluminium-
758 Hydroxid-Mineral. TMPM Tschermaks Mineralogische und Petrographische Mitteilungen 22,
759 79–87. https://doi.org/10.1007/BF01081303

760 Kumar, S., Sonat, C., Yang, E.-H., Unluer, C., 2020. Performance of reactive magnesia cement
761 formulations containing fly ash and ground granulated blast-furnace slag. Construction and
762 Building Materials 232, 117275. https://doi.org/10.1016/j.conbuildmat.2019.117275

763 Lahalle, H., 2016. Conditionnement de l'aluminium métallique dans les ciments phospho-magnésiens,
764 Thèse en Chimie-Physique, Université de Bourgogne Franche - Comté.

765 Lahalle, H., Cau Dit Coumes, C., Mercier, C., Lambertin, D., Cannes, C., Delpech, S., Gauffinet, S.,
766 2018. Influence of the w/c ratio on the hydration process of a magnesium phosphate cement and
767 on its retardation by boric acid. Cement and Concrete Research 109, 159–174.
768 https://doi.org/10.1016/j.cemconres.2018.04.010

769 Lahalle, H., Patapy, C., Glid, M., Renaudin, G., Cyr, M., 2019. Microstructural evolution/durability of
770 magnesium phosphate cement paste over time in neutral and basic environments. Cement and

771 Concrete Research 122, 42–58. https://doi.org/10.1016/j.cemconres.2019.04.011

772 Langton, C., Stefanko, D., 2011. Magnesium Mono Potassium Phosphate Grout For P-reactor Vessel
773 In-Situ Decomissioning. Aiken, SC (United States). https://doi.org/10.2172/1011325

774 Le Rouzic, M., Chaussadent, T., Stefan, L., Saillio, M., 2017. On the influence of Mg/P ratio on the
775 properties and durability of magnesium potassium phosphate cement pastes. Cement and
776 Concrete Research 96, 27–41. https://doi.org/10.1016/j.cemconres.2017.02.033

777 Li, C., Li, Y., Sun, H., Li, L., 2011. The Composition of Fly Ash Glass Phase and Its Dissolution
778 Properties Applying to Geopolymeric Materials. Journal of the American Ceramic Society 94,
779 1773–1778. https://doi.org/10.1111/j.1551-2916.2010.04337.x

780 Li, J., Zhang, W., Cao, Y., 2014. Laboratory evaluation of magnesium phosphate cement paste and
781 mortar for rapid repair of cement concrete pavement. Construction and Building Materials 58,
782 122–128. https://doi.org/10.1016/j.conbuildmat.2014.02.015

783 Lothenbach, B., Xu, B., Winnefeld, F., 2019. Thermodynamic data for magnesium (potassium)
784 phosphates. Applied Geochemistry 111, 104450.
785 https://doi.org/10.1016/j.apgeochem.2019.104450

786 Massiot, D., Fayon, F., Capron, M., King, I., Le Calvé, S., Alonso, B., Durand, J.-O., Bujoli, B., Gan,
787 Z., Hoatson, G., 2002. Modelling one- and two-dimensional solid-state NMR spectra. Magnetic
788 Resonance in Chemistry 40, 70–76. https://doi.org/10.1002/mrc.984

789 Neithalath, N., Weiss, J., Olek, J., 2006. Characterizing Enhanced Porosity Concrete using electrical
790 impedance to predict acoustic and hydraulic performance. Cement and Concrete Research 36,
791 2074–2085. https://doi.org/10.1016/j.cemconres.2006.09.001

792 Nied, D., Enemark-Rasmussen, K., L'Hopital, E., Skibsted, J., Lothenbach, B., 2016. Properties of
793 magnesium silicate hydrates (M-S-H). Cement and Concrete Research 79, 323–332.
794 https://doi.org/10.1016/j.cemconres.2015.10.003

795 Penel, G., Leroy, G., Rey, C., Bres, E., 1998. MicroRaman spectral study of the PO4 and CO3
796 vibrational modes in synthetic and biological apatites. Calcified Tissue International 63, 475–
797 481. https://doi.org/10.1007/s002239900561

798 Perona, R., Fernández-García, C., García-Lodeiro, I., Criado, M., Bastidas, J.M., Alonso, M.C., 2023.
799 Corrosion behavior and immobilization of pure aluminum and Al−Mg alloy LLRW in
800 magnesium potassium phosphate cements. Journal of Nuclear Materials 582, 154501.
801 https://doi.org/10.1016/j.jnucmat.2023.154501

802 Poras, G., Cau Dit Coumes, C., Antonucci, P., Cannes, C., Delpech, S., Perrin, S., 2023.
803 Electrochemical Behavior of Al/Mg Alloys Immobilized in a Magnesium Potassium Phosphate
804 Cement-Based Mortar. Materials 16. https://doi.org/10.3390/ma16155415

805 Pyo, J.Y., Um, W., Heo, J., 2021. Magnesium potassium phosphate cements to immobilize radioactive
806 concrete wastes generated by decommissioning of nuclear power plants. Nuclear Engineering
807 and Technology 53, 2261–2267. https://doi.org/10.1016/j.net.2021.01.005

808 Roosz, C., Grangeon, S., Blanc, P., Montouillout, V., Lothenbach, B., Henocq, P., Giffaut, E.,
809 Vieillard, P., Gaboreau, S., 2015. Crystal structure of magnesium silicate hydrates (M-S-H): The
810 relation with 2:1 Mg–Si phyllosilicates. Cement and Concrete Research 73, 228–237.
811 https://doi.org/10.1016/j.cemconres.2015.03.014

812 Roufosse, A.H., Aue, W.P., Roberts, J.E., Glimcher, M.J., Griffin, R.G., 1984. Investigation of
813 mineral phases of bone by solid-state phosphorus-31 magic-angle sample-spinning nuclear
814 magnetic resonance. Biochemistry 23, 6115–6120. https://doi.org/10.1021/bi00320a033

815 Schneider, H., Schreuer, J., Hildmann, B., 2008. Structure and properties of mullite—A review.
816 Journal of the European Ceramic Society 28, 329–344.
817 https://doi.org/10.1016/j.jeurceramsoc.2007.03.017

818 Seehra, S.S., Gupta, S., Kumar, S., 1993. Rapid setting magnesium phosphate cement for quick repair

of concrete pavements - characterisation and durability aspects. Cement and Concrete Research 23, 254–266. https://doi.org/10.1016/0008-8846(93)90090-V

Snellings, R., Chwast, J., Cizer, Ö., De Belie, N., Dhandapani, Y., Durdzinski, P., Elsen, J., Haufe, J., Hooton, D., Patapy, C., Santhanam, M., Scrivener, K., Snoeck, D., Steger, L., Tongbo, S., Vollpracht, A., Winnefeld, F., Lothenbach, B., 2018. RILEM TC-238 SCM recommendation on hydration stoppage by solvent exchange for the study of hydrate assemblages. Materials and Structures/Materiaux et Constructions 51. https://doi.org/10.1617/s11527-018-1298-5

Stoll, W.R., Neuman, W.F., 1956. The Uptake of Sodium and Potassium Ions by Hydrated Hydroxyapatite. Journal of the American Chemical Society 78, 1585–1588. https://doi.org/10.1021/ja01589a022

Torras, J., Buj, I., Rovira, M., de Pablo, J., 2011. Semi-dynamic leaching tests of nickel containing wastes stabilized/solidified with magnesium potassium phosphate cements. Journal of Hazardous Materials 186, 1954–1960. https://doi.org/10.1016/j.jhazmat.2010.12.093

Tropp, J., Blumenthal, N.C., Waugh, J.S., 1983. Phosphorus NMR study of solid amorphous calcium phosphate. Journal of the American Chemical Society 105, 22–26. https://doi.org/10.1021/ja00339a006

van der Lee, J., De Windt, L., Lagneau, V., Goblet, P., 2003. Module-oriented modeling of reactive transport with HYTEC. Computers & Geosciences 29, 265–275. https://doi.org/10.1016/S0098-3004(03)00004-9

Viani, A., Mácová, P., Sotiriadis, K., 2021. Amorphous-crystalline transformation control on the microstructural evolution of magnesium phosphate cements. Materials Letters 292, 129630. https://doi.org/10.1016/j.matlet.2021.129630

Viani, A., Mali, G., Mácová, P., 2017. Investigation of amorphous and crystalline phosphates in magnesium phosphate ceramics with solid-state 1H and 31P NMR spectroscopy. Ceramics

International 43, 6571–6579. https://doi.org/10.1016/j.ceramint.2017.02.087

Vieillard, P., Tardy, Y., 1984. Thermochemical Properties of Phosphates, in: Photosphate Minerals. Springer Berlin Heidelberg, Berlin, Heidelberg, pp. 171–198. https://doi.org/10.1007/978-3-642-61736-2_4

Wagh, A.S., 2013. Recent Progress in Chemically Bonded Phosphate Ceramics. ISRN Ceramics 2013, 1–20. https://doi.org/10.1155/2013/983731

Wagh, A.S., Jeong, S.-Y., Singh, D., 1997. High Strength Phosphate Cement Using, in: Proceedings of the 1st International Conference on High Strength Concrete. pp. 542–553.

Wang, T., Ishida, T., Gu, R., 2020. A study of the influence of crystal component on the reactivity of low-calcium fly ash in alkaline conditions based on SEM-EDS. Construction and Building Materials 243, 118227. https://doi.org/10.1016/j.conbuildmat.2020.118227

Weill, B., Bradik, J., 1988. US Patent n°4,756,762 - Magnesium phosphate cement systems.

Weng, Y., Ruan, S., Li, M., Mo, L., Unluer, C., Tan, M.J., Qian, S., 2019. Feasibility study on sustainable magnesium potassium phosphate cement paste for 3D printing. Construction and Building Materials 221, 595–603. https://doi.org/10.1016/j.conbuildmat.2019.05.053

Wilson, R.M., Elliott, J.C., Dowker, S.E.P., Rodriguez-Lorenzo, L.M., 2005. Rietveld refinements and spectroscopic studies of the structure of Ca-deficient apatite. Biomaterials 26, 1317–1327. https://doi.org/10.1016/j.biomaterials.2004.04.038

Xu, B., Coumes, C.C.D., Lambertin, D., Lothenbach, B., 2023. Compressive strength and hydrate assemblages of wollastonite-blended magnesium potassium phosphate cements exposed to different pH conditions. Cement and Concrete Composites 143. https://doi.org/10.1016/j.cemconcomp.2023.105255

Xu, B., Lothenbach, B., Leemann, A., Winnefeld, F., 2018. Reaction mechanism of magnesium

potassium phosphate cement with high magnesium-to-phosphate ratio. Cement and Concrete Research 108, 140–151. https://doi.org/10.1016/j.cemconres.2018.03.013

Xu, B., Lothenbach, B., Winnefeld, F., 2020. Influence of wollastonite on hydration and properties of magnesium potassium phosphate cements. Cement and Concrete Research 131, 106012. https://doi.org/10.1016/j.cemconres.2020.106012

Xu, B., Winnefeld, F., Kaufmann, J., Lothenbach, B., 2019. Influence of magnesium-to-phosphate ratio and water-to-cement ratio on hydration and properties of magnesium potassium phosphate cements. Cement and Concrete Research 123, 105781. https://doi.org/10.1016/j.cemconres.2019.105781

Xu, B., Winnefeld, F., Lothenbach, B., 2021. Effect of temperature curing on properties and hydration of wollastonite blended magnesium potassium phosphate cements. Cement and Concrete Research 142, 106370. https://doi.org/10.1016/j.cemconres.2021.106370

Xu, B., Winnefeld, F., Ma, B., Rentsch, D., Lothenbach, B., 2022. Influence of aluminum sulfate on properties and hydration of magnesium potassium phosphate cements. Cement and Concrete Research 156, 106788. https://doi.org/10.1016/j.cemconres.2022.106788

Yang, H., Martinelli, L., Tasso, F., Sprocati, A.R., Pinzari, F., Liu, Z., Downs, R.T., Sun, H.J., 2014. A new biogenic, struvite-related phosphate, the ammonium-analog of hazenite, (NH4)NaMg2(PO4)2.14H2O. American Mineralogist 99, 1761–1765. https://doi.org/10.2138/am.2014.4768

Yang, H., Sun, H.J., 2004. Crystal structure of a new phosphate compound, Mg2KNa(PO4)2·14H2O. Journal of Solid State Chemistry 177, 2991–2997. https://doi.org/10.1016/j.jssc.2004.05.008

Yang, H., Sun, H.J., Downs, R.T., 2011. Hazenite, KNaMg2(PO4)2·14H2O, a new biologically related phosphate mineral, from Mono Lake, California, U.S.A. American Mineralogist 96, 675–681. https://doi.org/10.2138/am.2011.3668

Yang, Q., Zhu, B., Wu, X., 2000. Characteristics and durability test of magnesium phosphate cement-based material for rapid repair of concrete. Materials and Structures/Materiaux et Constructions 33, 229–234. https://doi.org/10.1007/bf02479332

Yu, Y., Wang, J., Liu, C., Zhang, B., Chen, H., Guo, H., Zhong, G., Qu, W., Jiang, S., Huang, H., 2010. Evaluation of inherent toxicology and biocompatibility of magnesium phosphate bone cement. Colloids and Surfaces B: Biointerfaces 76, 496–504. https://doi.org/10.1016/j.colsurfb.2009.12.010

Yu, Y., Xu, C., Dai, H., 2016. Preparation and characterization of a degradable magnesium phosphate bone cement. Regenerative Biomaterials 3, 231–237. https://doi.org/10.1093/rb/rbw024

Zhang, X.-J., Lin, D.-Y., Yan, X.-H., Wang, X.-X., 2011. Evolution of the magnesium incorporated amorphous calcium phosphate to nano-crystallized hydroxyapatite in alkaline solution. Journal of Crystal Growth 336, 60–66. https://doi.org/10.1016/j.jcrysgro.2011.09.039

Zhang, Z., Yang, Z., Chen, Z., Kang, T., Ding, X., Li, Y., Liao, Y., Chen, C., Yuan, H., Peng, H., 2018. A study on bone cement containing magnesium potassium phosphate for bone repair. Cogent Biology 4, 1487255. https://doi.org/10.1080/23312025.2018.1487255

Zhao, Z., Chen, M., Xu, J., Li, L., Huang, Y., Yang, L., Zhao, P., Lu, L., 2021. Mix design and rheological properties of magnesium potassium phosphate cement composites based on the 3D printing extrusion system. Construction and Building Materials 284, 122797. https://doi.org/10.1016/j.conbuildmat.2021.122797